Weak gravitational lensing in different cosmologies, using an algorithm for shear in three dimensions

Andrew J. Barber,[1]★ Peter A. Thomas,[1] H. M. P. Couchman[2] and C. J. Fluke[3]

[1]*Astronomy Centre, University of Sussex, Falmer, Brighton BN1 9QJ*
[2]*Department of Physics and Astronomy, McMaster University, Hamilton, Ontario L8S 4M1, Canada*
[3]*Centre for Astrophysics and Supercomputing, Swinburne University, Melbourne, Australia*

ABSTRACT

We present the results of weak gravitational lensing statistics in four different cosmological *N*-body simulations. The data have been generated using an algorithm for the three-dimensional shear, which makes use of a variable softening facility for the *N*-body particle masses, and enables a physical interpretation for the large-scale structure to be made. Working in three dimensions also allows the correct use of the appropriate angular diameter distances.

Our results are presented on the basis of the filled-beam approximation in view of the variable particle softening scheme in our algorithm. The importance of the smoothness of matter in the Universe for the weak lensing results is discussed in some detail.

The low-density cosmology with a cosmological constant appears to give the broadest distributions for all the statistics computed for sources at high redshifts. In particular, the range in magnification values for this cosmology has implications for the determination of the cosmological parameters from high-redshift type Ia supernovae. The possibility of determining the density parameter from the non-Gaussianity in the probability distribution for the convergence is discussed.

Key words: methods: numerical – galaxies: clusters: general – cosmology: miscellaneous – gravitational lensing – large-scale structure of Universe.

1 INTRODUCTION

1.1 Outline

We present the results of a study of the weak gravitational lensing of light in four different cosmological models, using the algorithm for the three-dimensional shear developed by Couchman, Barber & Thomas (1999). Since weak lensing effects depend on the angular diameter distances for the lenses and sources, and also the specific distribution and evolution of matter, the results are sensitive to the particular cosmological model.

In *strong* lensing studies, frequent use is made of the 'thin-screen approximation', in which the mass distribution of the lens is projected along the line of sight and replaced by a mass sheet with the appropriate surface density profile. Deflections of the light from the source are then considered to take place only within the plane of the mass sheet, making computations for the light deflections simple. The simplicity of the thin-screen approximation has also lead to its frequent use in weak gravitational lensing studies, where each of the output volumes from

cosmological *N*-body simulations is treated as a planar projection of the particle distribution within it.

However, a number of problems can arise with two-dimensional approaches, especially in weak lensing studies in which the large-scale distribution of matter extending to high redshifts is responsible for the lensing. Couchman et al. (1999) considered some of the shortcomings, and were motivated to develop an algorithm to compute the six independent components in three dimensions of the second derivative of the gravitational potential (the three-dimensional shear). In the method used in the present work, for which the effects of lensing along lines of sight are required, the two-dimensional 'effective lensing potentials' (see Section 2) are obtained by integrating the computed three-dimensional shear components along the lines of sight. These effective lensing potentials are used to construct the Jacobian matrices which are recursively generated along the lines of sight, and from the final Jacobian matrices the magnifications and two-dimensional shear are determined.

A brief outline of this paper is as follows.

In Section 1.2 we summarize the previous weak gravitational lensing methods by other authors.

In Section 2, the essential equations for gravitational lensing are

★ E-mail: abarber@star.cpes.susx.ac.uk

explained, and the multiple lens-plane theory is described, culminating in expressions for the magnification, convergence, two-dimensional shear, and ellipticity, which are the weak lensing outputs from the cosmological simulations.

Section 3.1 summarizes the three-dimensional shear algorithm, and particularly the choice of the variable softening scale for the particles. This feature limits the effects of isolated particles (not representative of the large-scale structure), and builds in a physical significance both to the choice of the softening scale, and to the underlying form of the dark matter. We explain also how the softening carefully limits the incidence of strong lensing events in all the cosmologies. In Section 3.2 we describe the four cosmological N-body simulations used in this work. In Section 3.3 we state how the simulation boxes are oriented to minimize correlations in the large-scale structure between adjacent time-outputs, and we describe the establishment of lines of sight through the simulations, and the locations of the evaluation positions for the shear within them. In Section 3.4 we explain how the computed shear values are converted (after integration along the lines of sight) to physical units, and the approximations we have adopted in the method.

In Section 4.1 the Dyer–Roeder equation for the angular diameter distances is introduced, and Section 4.2 summarizes the results derived in Appendix A for the beam equation generalized for all the cosmologies. This precedes the discussion (Section 4.3) of magnifications obtainable in inhomogeneous universes with different degrees of smoothness, and highlights the significance of differences between researchers who adopt different approaches to this subject.

Section 5 formally presents the weak lensing results. We first (Section 5.1) attempt to see if the onset of structure formation can be seen from the shear data, and briefly comment on the expected behaviour of the developing shear. Secondly (Section 5.2), the results for magnification, convergence, shear and ellipticity are presented for all the cosmologies, compared and contrasted. We consider the impact of the smoothness parameter on the results.

It may be possible to determine the density parameter, Ω_0, from the probability distribution and the skewness in the distribution for the convergence, both of which may be measurable observationally. In Section 6.1 we present our results for these quantities, and compare them with others. The application to the determination of the cosmological parameters from type Ia supernovae is mentioned in Section 6.2.

In Section 7 the weak lensing statistics detailed in Section 5 are summarized, together with the results of the non-Gaussianity in the convergence.

We compare and contrast our results with other authors and present our conclusions in Section 8. Of particular significance are the common use of two-dimensional approaches by others, and the use of either point mass particles or particles with small softening scales, which introduce high values of magnification. These authors often use the empty-cone approximation, rather than the full-beam approximation, making comparisons difficult. This latter point is discussed.

In Appendix A we state the generalized beam equation, and derive the equations necessary for the numerical determination of the angular diameter distances for all the cosmologies.

1.2 Previous work

Numerous methods have been employed to study weak lensing, and throughout this paper we will make comparisons with previous work by other authors. We summarize here the methods which have been used by others.

Jaroszyński et al. (1990) use a 'ray-tracing' method to evaluate the matter column density in a matrix of 128^3 pixels for each of their lens-planes. The boxes were generated using a particle–mesh (PM) code in the standard cold dark matter (SCDM) cosmology, and were of side-dimension $128\,h^{-1}\,\mathrm{Mpc}$, where h is the Hubble constant in units of $100\,\mathrm{km\,s^{-1}\,Mpc^{-1}}$. By making use of the assumed periodicity in the particle distribution orthogonal to the line of sight, they translate the planes for each ray, so that it becomes centralized within the plane of one full period in extent. This removes any bias acting on the ray when the shear is computed. Instead of calculating the effect of every particle on the rays, the pixel column densities in the single period plane are used, and they assume that the matter in each of the pixels resides at the centre point of each pixel. They calculate the two two-dimensional components of the shear (see Section 2 for the definition of shear) as ratios of the mean convergence of the beam, which they obtain from the mean column density. However, they have not employed the net zero mean density requirement in the planes, (described in detail by Couchman et al. 1999), which ensures that deflections and shear can occur only when there are departures from homogeneity. Also, the matter in the pixel through which the ray is located is excluded. To follow the shearing across subsequent planes, they recursively generate the developing Jacobian matrix for each ray, in accordance with the multiple lens-plane theory (see Section 2).

Wambsganss, Cen & Ostriker (1998) also use the 'ray-tracing' method in cosmological N-body simulations. The method is applied to PM simulations of the SCDM cosmology, in which a convolution method is used to combine large-scale boxes of $400\,h^{-1}\,\mathrm{Mpc}$ and resolution $0.8\,h^{-1}\,\mathrm{Mpc}$, with small-scale boxes of $5\,h^{-1}\,\mathrm{Mpc}$ and the higher resolution of $10\,h^{-1}\,\mathrm{kpc}$. They randomly orient each simulation box, and project the matter contained within each on to a plane divided into pixels. They choose the central $8\,h^{-1}\,\mathrm{Mpc} \times 8\,h^{-1}\,\mathrm{Mpc}$ region through which to shoot rays, but account for the deflections of the rays in terms of all the matter in the plane of $80\,h^{-1}\,\mathrm{Mpc} \times 80\,h^{-1}\,\mathrm{Mpc}$. However, to speed up the computation, a hierarchical tree code in two dimensions is used to collect together those lenses (pixels) far away, whilst treating nearby lenses individually. The code assumes that all the matter in a pixel is located at its centre of mass. The matter in each pixel, which measures $10\,h^{-1}\,\mathrm{kpc} \times 10\,h^{-1}\,\mathrm{kpc}$, is assumed to be uniformly spread. By using the multiple lens-plane theory, they show both the differential magnification probability distribution, and the integrated one for 100 different source positions at redshift $z_s = 3.0$. One advantage of this type of ray-tracing procedure is its ability to indicate the possibility of multiple imaging, where different rays in the image plane can be traced back to the same pixel in the source plane, and they are able to compute the statistics of angular separations for multiple images.

Marri & Ferrara (1998) use lens-planes up to redshifts of $z = 10$ for mass distributions determined by the Press–Schechter formalism, and treat the particles as point-like masses with no softening. They apply their ray-tracing method to three cosmologies with $(\Omega_M, \Omega_\lambda, \Omega_\nu) = (1, 0, 0)$, $(0.4, 0.6, 0)$ and $(0.7, 0, 0.3)$. (Ω_M, Ω_λ and Ω_ν represent the density parameters for matter, vacuum energy and the hot dark matter component respectively.) The maximum number of lenses in a single plane is approximately 600, each having the appropriate computed mass value, and they follow 1.85×10^7 uniformly distributed rays within a solid angle

of 2.8×10^{-6} sr, corresponding to a $420 \times 420\,\text{arcsec}^2$ field. The final impact parameters of the rays are collected in an orthogonal grid of 300^2 pixels in the source plane. Because of the use of point masses, their method produces very high magnification values, greater than 30 for the Einstein–de Sitter cosmology. They have also chosen to use a smoothness parameter $\bar{\alpha} = 0$ in the redshift–angular diameter distance relation (described in Section 4) which depicts an entirely clumpy universe.

Jain, Seljak & White (1998; 2000) have made use of *N*-body simulations generated using a parallel adaptive particle–particle, particle–mesh (AP^{3}M) code. The cosmologies simulated are the same as the ones reported on here, but they have 256^3 particles and comoving box side dimensions of $85\,h^{-1}\,\text{Mpc}$ for their Einstein–de Sitter cosmologies, and $141\,h^{-1}\,\text{Mpc}$ for the open and cosmological constant models. For each plane, the projected density, together with the appropriate redshift-dependent factors, is Fourier-transformed, using periodic boundary conditions, to obtain the shear in Fourier space. The two-dimensional shear matrix is then computed on to a grid in real space by the inverse Fourier transform. The size of the grid is chosen to be compatible with the force-softening scale (the resolution) in the *N*-body simulations, so that for sources at redshifts around 1, the angular-scale size of the grid is less than, or of the same order as, the angular-scale size of the force-softening at these redshifts. Perturbations on the photon trajectories are computed and the shear matrix interpolated to the photon positions, enabling the Jacobian matrices to be computed by recursion. In view of the use of a fine grid for the shear and deflection angle computations, they are able to analyse their data on different scales, and are thus able to determine the power spectrum in both the shear and the convergence. This approach is very different from the approach we follow which makes use of variable softening for the particles depending on their particular environment, and which ensures that most 'rays' would pass entirely through regions of smoothed density, thereby requiring the application of the full-beam approximation. Jain et al. assume point particles interpolated on to their grid, and use the empty-cone approximation.

Hamana, Martel & Futamase (2000) study weak lensing in *N*-body simulations of three cosmologies with $(\Omega_0, \lambda_0, \sigma_8) = (1, 0, 1.2)$, $(0.3, 0.7, 0.85)$ and $(0.3, 0, 0.90)$. (We now use Ω_0 and λ_0 to represent the present matter density and vacuum energy density parameters respectively; σ_8 is the normalization on scales of $8\,h^{-1}\,\text{Mpc}$.) These were generated by a P^{3}M algorithm, using Fourier techniques on a 128^3 lattice. The comoving simulation box sizes were 128 Mpc, and the particles were given comoving softenings of 300 kpc. Three simulations were performed for each cosmological model, and boxes from the different simulations combined to limit correlations in large-scale structure between adjacent boxes. Each of the mass distributions in the simulation boxes were then projected on to planes at the box redshift, and Poisson's equation solved numerically on each of them. This was done by first evaluating the surface density on to a 512×512 grid, based on the particle positions, and then inverting Poisson's equation using a Fast Fourier Transform (FFT) method. As the multiple lens-plane theory was to be used for more than 10^7 rays passing through each plane, the recursion algorithm was simplified by assuming small deflections for the rays. This also meant that the rays could be considered to pass through the grid points, and travel, effectively, in straight lines through the entire distance from the observer to the source plane. We have also made this approximation in our own method.

An alternative to the conventional form of 'ray-tracing' was introduced by Refsdal (1970), who used 'ray-tracing' with calculations of the differential deflections of light rays around a central ray to determine the distribution of magnifications.

Fluke, Webster & Mortlock (1999, 2000) have developed this idea further as the 'ray-bundle' method. The principle is to trace the passage of a discrete bundle of light rays as it passes through the deflection planes. The advantage of the method is that it provides a direct comparison between the shape and size of the bundle at the observer and at the source plane, so that the magnification, ellipticity and rotation can be determined straightforwardly. The authors have selected a range of popular cosmologies, including the ones reported on here, and have produced their own *N*-body simulation data sets using a P^{3}M algorithm. For each cosmology they have produced a number of independent simulations to enable them to randomly choose a simulation box for a particular epoch from any of the realizations. In this way, correlations of large-scale structure between adjacent boxes are avoided. They have run their simulations with 64^3 dark matter particles, with box sizes ranging from $80\,h^{-1}\,\text{Mpc}$ to $164.3\,h^{-1}$ Mpc. Having randomly selected the boxes for a given cosmology, the particle mass distributions are then projected on to planes at the redshifts of the boxes. The authors construct approximately 50 000 bundles, each comprising eight rays, to shoot in random directions through the planes, from the observer's location at $z = 0$. The shooting area was limited to $50 \times 50\,\text{arcsec}^2$ to avoid edge effects of the planes, and only matter within a single period in the transverse direction is included in the planes. In addition, a radius, typically $15\,h^{-1}\,\text{Mpc}$ centred around each bundle, is chosen for the extent of the matter to be included in the deflection angle computations. The projected masses are also considered as point particles, so that very high magnification values can be achieved in principle; however, the authors do not include bundles which pass within $\sqrt{2}$ of the Einstein radius of any particle. Because of their use of point masses, they use the empty-cone approximation in the determination of the statistical distributions of magnifications for the different cosmological models.

Premadi, Martel & Matzner (1998a) have introduced individual galaxies into the computational volume, matching the two-point correlation function for galaxies. They also assign morphological types to the galaxies according to the individual environment, and apply a particular surface density profile for each. Five different sets of initial conditions were used for the simulations, so that the individual plane projections can be selected at random from any set. *N*-body simulations were produced for three cosmologies with $(\Omega_0, \lambda_0) = (1, 0)$, $(0.2, 0)$ and $(0.2, 0.8)$ in boxes of comoving side-dimension $128\,h^{-1}\,\text{Mpc}$. They solve the two-dimensional Poisson equation on a grid, and invert the equation using a FFT method to obtain the first and second derivatives of the gravitational potential on each plane. They also correctly ensure that the mean surface density in each lens-plane vanishes, so that a good interpretation of the effects of the background matter is made. Their method uses beams of light, each comprising 65 rays arranged in two concentric rings of 32 rays each, plus a central ray. The multiple lens-plane theory then enables the distributions of cumulative magnifications to be obtained.

Tomita (1998a,b) also uses a ray bundle method, but by evaluating the gravitational potential at approximately 3000 locations between the observer and sources at redshift 5, he is able to compute the weak lensing statistics without using the multiple lens-plane theory. He has used *N*-body simulations produced using a tree code with 32^3 particles in four different cosmologies with $(\Omega_0, \lambda_0) = (1, 0)$, $(0.2, 0.8)$, $(0.2, 0)$ and $(0.4, 0)$.

In all of these, except the SCDM cosmology ($\Omega_0 = 1$, $\lambda_0 = 0$), the particles are treated as galaxy-size objects. In the SCDM cosmology, 20 per cent of the particles are treated thus, whilst 80 per cent are given softening radii of $100\,h^{-1}\,\mathrm{kpc}$ (model a), $40\,h^{-1}\,\mathrm{kpc}$ (model b) and $20\,h^{-1}\,\mathrm{kpc}$ (model c). Ray bundles are formed from 5×5 rays arranged in a square, with separation angles (fixed for each run) at between 2 arcsec and 1 deg. At each of the 3000 positions between the observer and source, the potential is evaluated at each ray position by translating each simulation cube (using the periodic properties) so that the centre of each bundle is located in the centre of each cube. In this way, all the matter within a full period in extent contributes to the calculation of the potential (although no account is taken of matter beyond one period transverse to the line of sight). To avoid spurious values of the potential arising from masses close to evaluation positions, an average of the potential is taken by integrating it analytically over the interval between adjacent evaluation positions. The light propagation is then determined by solving the null-geodesic equations, and the required statistics constructed from shooting 1000 bundles through the flat cosmologies, and 200 bundles through the open cosmologies.

2 THE PROPAGATION OF LIGHT

In the case of multiple deflections of light by a series of projected lens-planes, the Jacobian matrix develops in accordance with the multiple lens-plane theory, which has been summarized by Schneider, Ehlers & Falco (1992). Its form at redshift $z = 0$ enables all the lensed properties of light from distant sources to be determined.

We follow, in outline, their description. For a system of N lenses, the basic lens equation for a single lens, relating the angular position of the source to that of the image, may be generalized straightforwardly. If the position vector of the source in the plane perpendicular to the line of sight at the source position (the source plane) is $\boldsymbol{\eta}$, and the position vectors of the image positions in the various, N, deflection planes are $\boldsymbol{\xi}_i$, where $i = 1, \dots, N$, then the lens equation may be written as

$$\boldsymbol{\eta} = \frac{D_s}{D_1}\boldsymbol{\xi}_1 - \sum_{i=1}^{N} D_{is}\hat{\boldsymbol{\alpha}}_i(\boldsymbol{\xi}_i), \tag{1}$$

where D_i is the angular diameter distance to the ith lens, D_{is} is that from the ith lens to the source, and $\hat{\boldsymbol{\alpha}}_i$ is the deflection angle at the ith lens. To make equation (1) dimensionless, put

$$\boldsymbol{x}_i = \boldsymbol{\xi}_i / D_i, \tag{2}$$

and for the source,

$$\boldsymbol{y} = \boldsymbol{x}_{N+1} = \boldsymbol{\eta}/D_s = \boldsymbol{\eta}/D_{N+1}. \tag{3}$$

We also use the individual reduced deflection angles defined by

$$\boldsymbol{\alpha}_i = \frac{D_{is}}{D_s}\hat{\boldsymbol{\alpha}}_i. \tag{4}$$

Then the displacement in the jth lens plane is

$$\boldsymbol{x}_j = \boldsymbol{x}_1 - \sum_{i=1}^{j-1}\frac{D_{ij}}{D_j}\hat{\boldsymbol{\alpha}}_i(D_i\boldsymbol{x}_i) = \boldsymbol{x}_1 - \sum_{i=1}^{j-1}\frac{D_s}{D_{is}}\frac{D_{ij}}{D_j}\boldsymbol{\alpha}_i(D_i\boldsymbol{x}_i), \tag{5}$$

or

$$\boldsymbol{x}_j = \boldsymbol{x}_1 - \sum_{i=1}^{j-1}\beta_{ij}\boldsymbol{\alpha}_i(D_i\boldsymbol{x}_i), \tag{6}$$

where

$$\beta_{ij} \equiv \frac{D_s}{D_{is}}\frac{D_{ij}}{D_j}. \tag{7}$$

Then the full form of the ray-tracing equation is equation (6) evaluated at the source plane:

$$\boldsymbol{y} = \boldsymbol{x}_1 - \sum_{i=1}^{N}\boldsymbol{\alpha}_i. \tag{8}$$

(The β_{ij} factor disappears, because $\beta_{is} = 1$ from its definition.) The mapping of the source on to the image is given by the Jacobian matrix, which relates small changes in the source to corresponding small changes in the image seen on the first lens-plane:

$$\mathcal{A} \equiv \frac{\partial \boldsymbol{y}}{\partial \boldsymbol{x}_1}. \tag{9}$$

Similarly, we may define Jacobian matrices appropriately at each of the lens-planes:

$$\mathcal{A}_i \equiv \frac{\partial \boldsymbol{x}_i}{\partial \boldsymbol{x}_1}. \tag{10}$$

We now define the derivative of the reduced deflection angle for the ith lens by

$$\mathcal{U}_i \equiv \frac{\partial \boldsymbol{\alpha}_i}{\partial \boldsymbol{x}_i}. \tag{11}$$

By defining the 'effective lensing potential' in terms of the angular position, $\boldsymbol{\theta}_i$ for the ith lens as an integral along the line-of-sight direction, x_3,

$$\psi_i(\boldsymbol{\theta}_i) = \frac{D_{ds}}{D_d D_s}\frac{2}{c^2}\int \phi(D_d\boldsymbol{\theta}_i, x_3)\,\mathrm{d}x_3, \tag{12}$$

in which c is the velocity of light, $\mathcal{U}_i$ can be shown to be equivalent to the matrix of the second derivatives of the effective lensing potential for the ith lens, and is therefore related to the second derivative of the gravitational potential (the shear):

$$\mathcal{U}_i = \begin{pmatrix} \psi_{11}^i & \psi_{12}^i \\ \psi_{21}^i & \psi_{22}^i \end{pmatrix}, \tag{13}$$

where the superscripts, i, denote the deflection plane index, and where we have written

$$\psi_{11} \equiv \frac{\partial^2 \psi(\boldsymbol{\theta})}{\partial \theta_1^2}, \quad \psi_{12} \equiv \frac{\partial^2 \psi(\boldsymbol{\theta})}{\partial \theta_1 \partial \theta_2}, \tag{14}$$

$$\psi_{21} \equiv \frac{\partial^2 \psi(\boldsymbol{\theta})}{\partial \theta_2 \partial \theta_1}, \quad \text{and} \quad \psi_{22} \equiv \frac{\partial^2 \psi(\boldsymbol{\theta})}{\partial \theta_2^2}, \tag{15}$$

in which the suffixes in the denominators refer to the coordinate directions. Then the ray-tracing equation (8) gives

$$\mathcal{A}_{\text{total}} \equiv \frac{\partial \boldsymbol{y}}{\partial \boldsymbol{x}_1} = \mathcal{I} - \sum_{i=1}^{N}\frac{\partial \boldsymbol{\alpha}_i}{\partial \boldsymbol{x}_1} = \mathcal{I} - \sum_{i=1}^{N}\frac{\partial \boldsymbol{\alpha}_i}{\partial \boldsymbol{x}_i}\frac{\partial \boldsymbol{x}_i}{\partial \boldsymbol{x}_1}$$

$$= \mathcal{I} - \sum_{i=1}^{N}\mathcal{U}_i\mathcal{A}_i, \tag{16}$$

where $\mathcal{I}$ is the identity matrix.

Thus the final Jacobian matrix can be evaluated at $z = 0$, since the individual matrices can be obtained by recursion. Using equation (6), they are just

$$\mathcal{A}_j = \mathcal{I} - \sum_{i=1}^{j-1}\beta_{ij}\mathcal{U}_i\mathcal{A}_i \tag{17}$$

for the jth lens, and

$$\mathcal{A}_1 = \mathcal{I}. \tag{18}$$

In our approach, the second derivatives of the two-dimensional effective lensing potentials required for each deflection location, are obtained by integration of the computed three-dimensional shear values, i.e., the second derivatives of the *peculiar* gravitational potential. It is necessary to work with the peculiar gravitational potential, because the shearing of light arises from deviations from homogeneity; in a pure Robertson–Walker universe we would expect no deviations. Couchman et al. (1999) derive the expression for the peculiar gravitational potential, ϕ, in terms of the gravitational potential, Φ, and the mean density, $\bar{\rho}$:

$$\phi = \Phi - 2/3\pi G a^2 \bar{\rho} x^2; \tag{19}$$

G is the universal gravitational constant, x is the position vector, and a is the expansion factor for the universe (so that ax is the comoving position vector). This result corresponds to a system with zero net mass on large scales and immediately gives

$$\frac{\partial \phi}{\partial x_i} = \frac{\partial \Phi}{\partial x_i} - 4/3\pi G a^2 \bar{\rho} x_i \tag{20}$$

and

$$\frac{\partial^2 \phi}{\partial x_i \partial x_j} = \frac{\partial^2 \Phi}{\partial x_i \partial x_j} - 4/3\pi G a^2 \bar{\rho} \delta_{ij}. \tag{21}$$

Equation (21) shows how the real result for the shear, $\partial^2 \phi/\partial x_i \partial x_j$, based on the peculiar gravitational potential, is related to the value of $\partial^2 \Phi/\partial x_i \partial x_j$ through the subtraction of the term in the mean density.

Equation (21) can now be evaluated explicitly for the three-dimensional shear. The integral solution of Poisson's equation is well-known, and the solution can be easily differentiated twice to give

$$\frac{\partial^2 \phi(\boldsymbol{R})}{\partial x_i \partial x_j} = G \iiint \left[\frac{\rho(\boldsymbol{R}')}{|\boldsymbol{R} - \boldsymbol{R}'|^3} \delta_{ij} - \frac{3\rho(\boldsymbol{R}')(x_i - x_i')(x_j - x_j')}{|\boldsymbol{R} - \boldsymbol{R}'|^5} \right] d^3 R'$$
$$- 4/3\pi G a^2 \bar{\rho} \delta_{ij}. \tag{22}$$

(We have introduced $\boldsymbol{R}$ and $\boldsymbol{R}'$ for the evaluation position for the shear, and the matter positions respectively. In practice, of course, the triple integral over all space would be replaced by a summation.) The two-dimensional second derivatives of the effective lensing potentials required for the Jacobian matrices then follow immediately from equation (12) (using spatial rather than angular coordinates):

$$\psi_{ij} = \frac{D_d D_{ds}}{D_s} \cdot \frac{2}{c^2} \int \frac{\partial^2 \phi(x_3)}{\partial x_i \partial x_j} \, dx_3. \tag{23}$$

D_d, D_{ds}, and D_s are the angular diameter distances from the observer to the lens, the lens to the source, and the observer to the source, respectively. The integration is along the coordinate direction, x_3, and the subscripts i and j now refer to any of the three coordinate directions. This equation applies quite generally for any deflection location, so the deflection plane index has been dropped for clarity.

We now summarize the main equations we shall need for weak lensing, which are obtainable from the final Jacobian matrix. The final emergent magnification, μ, may be computed after passage

through an entire box or set of boxes, and is

$$\mu = (\det \mathcal{A})^{-1}. \tag{24}$$

The convergence, κ, is

$$\kappa = \tfrac{1}{2}(\psi_{11} + \psi_{22}), \tag{25}$$

and is therefore obtainable from the diagonal elements of the Jacobian matrix.

The two-dimensional shear, γ, in each line of sight, is given by

$$\gamma^2 \equiv \tfrac{1}{4}(\psi_{11} - \psi_{22})^2 + \psi_{12}^2. \tag{26}$$

(We may take $\psi_{12} = \psi_{21}$, because we are dealing with a weak shear field which is smoothed by the variable particle softening, ensuring that the gravitational potential and its derivatives are well-behaved continuous functions.)

From equation (24), and these definitions,

$$\mu = (1 - \psi_{11} - \psi_{22} + \psi_{11}\psi_{22} - \psi_{12}^2)^{-1}, \tag{27}$$

or

$$\mu = \frac{1}{(1 - \kappa)^2 - \gamma^2}. \tag{28}$$

In the presence of convergence and shear, a circular source becomes elliptical in shape, and the ellipticity, ϵ, defined in terms of the ratio of the minor and major axes, becomes

$$\epsilon = 1 - \frac{1 - \kappa - \gamma}{1 - \kappa + \gamma}, \tag{29}$$

which reduces to

$$\epsilon \simeq 2\gamma(1 + \kappa - \gamma) + O(\kappa^3, \gamma^3) \tag{30}$$

in weak lensing.

In our method, the evaluation of the second derivatives of the two-dimensional effective lensing potentials is obtained from integration of the computed three-dimensional shear values at a large number of evaluation positions along lines of sight. The multiple lens-plane theory then enables distributions of the magnification, ellipticity, convergence and shear at redshift $z = 0$ to be computed for light rays traversing the set of linked simulation boxes starting from the chosen source redshift. The ability to apply the appropriate angular diameter distances at every evaluation position avoids the introduction of errors associated with planar methods, and also allows the possibility of choosing source positions within a simulation box if necessary.

3 PROCEDURE

3.1 The three-dimensional shear algorithm

Couchman et al. (1999) describe in detail the algorithm for the computation of the elements of the matrix of second derivatives of the gravitational potential. The algorithm is based on the standard P^{3}M method (see Hockney & Eastwood 1988), and uses an FFT convolution method. It computes all of the six independent shear component values at each of a large number of selected evaluation positions within a three-dimensional N-body particle simulation box. It has a computational cost of order $N \log_2 N$, where N is the number of particles in the simulation volume, and for ensembles of particles, used in typical N-body simulations, the rms errors in the computed shear component values are typically ~ 0.3 per cent. In addition, the shear algorithm has the following features.

(A) The algorithm uses variable softening designed to distribute the mass of each particle within a radial profile depending on its specific environment. By virtue of this facility, we have been able to choose the softening such that light rays feel the existence of a smooth mass distribution. Each particle may be assigned its own softening-scale parameter, depending on the particle number-density in its environment. In this way, it can be used to minimize the effects of isolated single particles, whilst the smoothed denser regions are able to represent the form of the large-scale structure. The parameter we have chosen to delineate the softening scale for each particle is proportional to l, where $2l$ is the radial distance to the particle's 32nd nearest neighbour. The value of l has been evaluated for every particle by using a smoothed particle hydrodynamics (SPH) density program for each simulation box, and is read in by the shear code along with the particle position coordinates.

The maximum softening is allowed to be of the order of the mesh dimension for isolated particles, which is defined by the regular grid laid down to decompose the short- and long-range force calculations. In this way, individual isolated particles are unable to strongly influence the computed shear values, in accordance with our need to study the broad properties of the large-scale structure, rather than the effects of individual particles, which are not representative of physical objects.

For the minimum softening scale we wanted the softening to reflect the large-scale structure in the simulations, and so we based our choice on estimates of the Einstein radii for large clusters of particles. Using the dimensionless angular diameter distances in terms of the present value of the Hubble parameter, H_0, i.e., r_d $\left(\equiv \frac{H_0}{c}D_d\right)$, r_{ds} $\left(\equiv \frac{H_0}{c}D_{ds}\right)$, and r_s $\left(\equiv \frac{H_0}{c}D_s\right)$, for the observer to the lens, the lens to the source, and the observer to the source, respectively, the Einstein radius, R_E, becomes

$$R_E = 8.6 \times 10^{-3}\, h^{-1} N^{\frac{1}{2}} \left(\frac{r_d r_{ds}}{r_s}\right)^{\frac{1}{2}} \text{Mpc} \tag{31}$$

for a cluster of N particles, each of mass $1.29 \times 10^{11}\,\text{M}_\odot$ (see Section 3.2), where h is the Hubble parameter in units of $100\,\text{km s}^{-1}\text{Mpc}^{-1}$. Substituting values for the angular diameter distance factors then gives a maximum value of $R_E = 2.84 \times 10^{-3}\,h^{-1}N^{\frac{1}{2}}$ Mpc for a source at redshift $z_s = 1$ in the SCDM cosmology. This occurs for a lens at redshift $z_d = 0.29$. Thus, for a cluster of 1000 particles, $R_E = 0.089\,h^{-1}$ Mpc. For a source at redshift 3.6, the maximum value of R_E is $0.108\,h^{-1}$ Mpc and occurs for a lens at redshift 0.53. Following this approach, we therefore set a working minimum value for the variable softening of $0.1\,h^{-1}$ Mpc, equivalent to $10^{-3} \times (1 + z)$ in box units, where z is the box redshift.

The corresponding values for R_E in the other cosmologies, for $N = 1000$, are as follows.

For $\Omega_0 = 0.3$, $\lambda_0 = 0$, the maximum value of R_E is $0.093\,h^{-1}$ Mpc for $z_s = 1$, and occurs for $z_d = 0.32$. For $z_s = 3.6$, the maximum value of R_E is $0.115\,h^{-1}$ Mpc, and occurs for $z_d = 0.58$.

For $\Omega_0 = 0.3$, $\lambda_0 = 0.7$, the maximum value of R_E is $0.104\,h^{-1}$ Mpc for $z_s = 1$, and occurs for $z_d = 0.36$. For $z_s = 3.6$, the maximum value of R_E is $0.142\,h^{-1}$ Mpc, and occurs for $z_d = 0.67$.

Consequently, we used throughout a minimum softening of $0.1\,h^{-1}$ Mpc which is always greater than, or similar to, the maximum value of the Einstein radius for a cluster of 1000 particles. At the same time, the softening scale is approximately of galactic dimensions, giving a realistic interpretation to the choice. We have also accounted for the effects of the different numbers of particles per box in the different cosmological simulations. The variable softening scale for each particle has been retained at the same level in all the cosmologies, so that the same mass value is contained within it. Thus, around small-particle clusters there would be differences in the softening from cosmology to cosmology, but around large clusters, where the shearing is likely to be most important, the differences would be tiny.

Couchman et al. (1999) have investigated the sensitivity of weak lensing results to the input softening, finding differences only in limited numbers of lines of sight at the high-magnification end of the distributions.

(B) The shear algorithm works within three-dimensional simulation volumes, rather than on planar projections of the particle distributions, so that angular diameter distances to every evaluation position can be applied. It has been shown (Couchman et al. 1999) that in specific circumstances, the results of two-dimensional planar approaches are equivalent to three-dimensional values integrated throughout the depth of a simulation box, provided the angular diameter distance is assumed constant throughout the depth. However, by ignoring the variation in the angular diameter distances throughout the box, errors up to a maximum of 9 per cent can be reached at a redshift of $z = 0.5$ for SCDM simulation cubes of comoving side $100\,h^{-1}$ Mpc. (Errors can be larger than this at high and low redshifts, but the angular diameter distance multiplying factor for the shear values is greatest here for sources we have chosen at a redshift of 4.)

(C) The shear algorithm automatically includes the contributions of the periodic images of the fundamental volume, essentially creating a realisation extending to infinity. Couchman et al. (1999) showed that it is necessary to include the effects of matter well beyond the fundamental volume in general (but depending on the particular particle distribution), to achieve accurate values for the shear. Methods which make use of only the matter within the fundamental volume may suffer from inadequate convergence to the limiting values.

(D) The method uses the peculiar gravitational potential, ϕ, through the subtraction of a term depending upon the mean density. Such an approach is equivalent to requiring that the net total mass in the system be set to zero, and ensures that we deal only with light ray deflections arising from departures from homogeneity.

3.2 The Hydra *N*-body simulations

The three-dimensional shear code can be applied to any three-dimensional distribution of point masses confined within a cubic volume, and produces shear values as if the fundamental volume were repeated indefinitely to represent a three-dimensional periodic distribution of masses. Each particle may be assigned an individual mass, although in the tests and our application of the code, all the particles were assumed to be dark matter particles with the same mass.

The code has been applied to the data bank of cosmological *N*-body simulations provided by the Hydra Consortium (http://hydra.mcmaster.ca/hydra/index.html) and produced using the 'Hydra' *N*-body hydrodynamics code (Couchman, Thomas & Pearce 1995). Simulations from four different cosmologies were used, which will be referred to as the SCDM, TCDM, OCDM and LCDM cosmologies. Each of the simulations used a cold dark matter-like spectrum, and the parameters used in the generation and specification of these cosmological simulations are listed in Table 1.

Table 1. Parameters used in the generation of the four different cosmological simulations. The individual particle masses, $M_{part} = 1.29 \times 10^{11} \, h^{-1} \, M_\odot$, are the same in all the cosmologies.

Cosmology	Ω_0	λ_0	Γ	σ_8	No. of particles	Box side (h^{-1} Mpc)
SCDM	1.0	0.0	0.50	0.64	128^3	100
TCDM	1.0	0.0	0.25	0.64	128^3	100
OCDM	0.3	0.0	0.25	1.06	86^3	100
LCDM	0.3	0.7	0.25	1.22	86^3	100

Ω_0 and λ_0 are the present-day values of the density parameter and the vacuum energy density parameter respectively, so that the SCDM and TCDM cosmologies are representative of Einstein–de Sitter universes, whereas the OCDM cosmology represents a low-density, open universe, and the LCDM a low-density, but spatially flat universe with a cosmological constant. The power spectrum shape parameter, Γ, is set to 0.5 in the SCDM cosmology, but the empirical determination (Peacock & Dodds 1994) of 0.25 for cluster scales has been used in the other cosmologies. In each case, the normalization, σ_8, on scales of $8 \, h^{-1}$ Mpc has been set to reproduce the number density of clusters (Viana & Liddle 1996). Since gravity-only simulations have been used, the value of the Hubble parameter is arbitrary.

In the SCDM and TCDM cosmologies, the number of particles is 128^3, leading to individual dark matter particle masses of $M_{part} = 1.29 \times 10^{11} \, h^{-1} \, M_\odot$. In the low-density universes, the number of particles is 0.3 times the number in the critical-density universes, leading to the same individual particle masses. The simulation output times were chosen so that consecutive simulation boxes may be snugly abutted; the side-dimensions are $100 \, h^{-1}$ Mpc in every case. Consequently, there are different numbers of time-outputs to a given redshift value for the different cosmologies. For a nominal source redshift of $z_s = 4$ (which is the furthest extent of our weak lensing analysis), 33 simulation boxes were abutted to a redshift of 3.90 in the SCDM cosmology, 33 to a redshift of 3.93 in the TCDM cosmology, 41 to a redshift of 4.00 in the OCDM cosmology, and 48 to a redshift of 3.57 in the LCDM cosmology. (The *number* of boxes has no bearing on the weak lensing statistics.)

3.3 Orientation and lines of sight

Each time-output in a given simulation run is generated using the same initial conditions, so that a particular structure (although evolving) occurs at the same location in all the boxes, and is therefore repeated with the periodicity of the box. To avoid such obvious and unrealistic correlations, we have arbitrarily translated, rotated (by multiples of 90°) and reflected each time-slice, about each coordinate axis, before linking them together to form the continuous depiction of the universe back to the source redshift.

To follow the behaviour of light rays from a distant source through the simulation boxes, and to obtain distributions of the properties at $z = 0$, we construct a regular rectangular grid of directions through each box. Since there are likely to be only small deflections, and the point of interest is the statistics of output values, each light ray is considered to follow one of the lines defined by these directions through the boxes. The evaluation positions are specified along each of these lines of sight.

We have selected 1000 evaluation positions on each of 100×100 lines of sight, which is well matched to the minimum variable softening, giving adequate sampling in the line-of-sight

direction; the method has been tested using up to a total of 4×10^6 lines of sight, and we have found that whilst using a larger number of lines of sight smoothes the distribution plots for the magnification and shear at the high-magnification end and gives rise to higher maximum values of the magnification, the statistical widths of the plots are virtually unchanged. Since we are dealing with weak lensing effects and are interested only in the statistical distribution of values, these lines of sight adequately represent the trajectories of light rays through each simulation box. It is sufficient also to connect each 'ray' with the corresponding line of sight through subsequent boxes in order to obtain the required statistics of weak lensing. This is justified because of the random re-orientation of each box performed before the shear algorithm is applied.

3.4 Conversion factors and approximations in the method

The second derivatives of the two-dimensional effective lensing potentials are obtained from the three-dimensional second derivatives of the peculiar gravitational potential by integration, in accordance with equation (23). The integration of the three-dimensional shear values has been made in small steps (0.02 of the box depth) along each line of sight, enabling the weak lensing properties to be determined from the Jacobian matrices and recorded at 50 evenly spaced locations along each line of sight in every simulation box. To evaluate the absolute second derivatives of the effective lensing potentials, the appropriate scaling factor is introduced, which applies to the simulation box dimensions. From equation 23, the factor $B(1 + z)^2 r_d r_{ds}/r_s$ can be extracted, where $B = (c/H_0)(2/c^2)GM_{part} \times$ (comoving box depth)$^{-2}$. For the simulation boxes used, which have comoving dimensions of $100 \, h^{-1}$ Mpc, $B = 3.733 \times 10^{-9}$, and the $(1 + z)^2$ factor occurs to convert the comoving code units into physical units. (The step length for the integrations in each box is left as a code parameter, so that it may be varied at will, although in the analysis reported here, the step length was invariably $0.02 \times$ the box depth.)

The procedure to obtain the two-dimensional second derivatives of the effective lensing potentials involves a number of approximations.

First, it is assumed that the angular diameter distances required for equation (23) vary linearly throughout each step length ($0.02 \times$ the box depth). They are, however, evaluated exactly at the 50 step positions through each box.

Second, in our approach we assume that, although each simulation box is generated as a single simulation output-time representation, the angular diameter distances vary throughout the depth of each box, as they would in the real Universe.

Third, as mentioned in the previous section, we assume only weak deflections for light rays, so that they are assumed to follow the straight lines of sight represented by the grid points of the evaluation positions. Since we are interested only in the statistics of lensing within large-scale structure simulations, this is a perfectly acceptable practice.

Finally, we have made use of a weak lensing approximation for the computation of the intermediate Jacobian matrices. The full form for the final Jacobian matrix (equation 16) is computed by recursion, by including the intermediate matrices given by equations (17) and (18). Expanding equation (16) fully involves second-order and higher order terms, arising from the cross multiplication of the intermediate Jacobian matrices, the distance factors represented by β_{ij}, and the matrices $\mathcal{U}_i$. For weak lensing in which all the ψ_{ij} are much less than unity, the full form for $\mathcal{A}_{total}$

simplifies considerably to

$$\mathcal{A}_{\text{total}} \simeq \mathcal{I} - \sum_{i=1}^{N} \mathcal{U}_i. \tag{32}$$

This is the form used; strong lensing events will still be recorded as such, but using this approximation, the component values in $\mathcal{A}_{\text{total}}$ will not be accurate in strong lensing cases. However, the incidence of strong lensing events is likely to be very small, because of our choice of the softening scale (see Section 4.3). This being the case, any strong lensing events will not adversely affect the weak lensing statistics determined in our analysis.

4 ANGULAR DIAMETER DISTANCES IN INHOMOGENEOUS UNIVERSES

4.1 The Dyer–Roeder equation

Our three-dimensional approach allows the use of the appropriate angular diameter distances at every single evaluation position. This is not possible in two-dimensional approaches, where it is assumed that all the lensing mass in a box is projected on to a plane at a single angular diameter distance.

Since the angular diameter distances depend very much on the distribution of matter and the particular cosmology, it is necessary to have available appropriate values for the angular diameter distances for the particular distribution of matter in the simulation data set being investigated.

By considering the universe to be populated by randomly distributed matter inhomogeneities, but resembling the Robertson-Walker, Friedmann–Lemaître model on large scales, a second-order differential equation is obtained for the angular diameter distance, D, in terms of the density parameter, Ω_0, for the universe, the vacuum energy density parameter, λ_0, and the redshift, z, of the source. Dyer & Roeder (1973) made assumptions about the type of matter distribution to obtain a more practical equation for $\lambda_0 = 0$ cosmologies. They assumed that a mass fraction, $\bar{\alpha}$ (called the smoothness parameter), of matter in the universe is smoothly distributed, and that the fraction $(1 - \bar{\alpha})$ is bound into clumps. Then the equation for the angular diameter distance (with $\lambda_0 = 0$) is:

$$(z + 1)\,(\Omega_0 z + 1)\frac{\mathrm{d}^2 D}{\mathrm{d}z^2} + \left(\frac{7}{2}\Omega_0 z + \frac{\Omega_0}{2} + 3\right)\frac{\mathrm{d}D}{\mathrm{d}z}$$

$$+ \left[\frac{3}{2}\bar{\alpha}\Omega_0 + \frac{|\sigma|^2}{(1+z)^5}\right] D = 0, \tag{33}$$

in which σ is the optical scalar for the shear, introduced by the matter distribution around the beam.

In order to apply equation (33), Dyer & Roeder (1973) considered the following scenarios. They considered a universe in which all the matter is bound into clumps, so that $\bar{\alpha} = 0$, and in which the light beam passes far away from the clumps. This is described as light propagating through an 'empty cone', and gives rise to maximal divergence of the beam. The opposite scenario has $\bar{\alpha} = 1$, i.e., an entirely smooth universe. Here the smooth matter distribution is present within the beam, giving a 'full cone', or 'filled beam' approximation.

We have considered whether the shear along individual lines of sight is able to significantly affect the chosen values for the angular diameter distances. Our work has been conducted using cosmological simulations in which the distributions of matter are

smooth, and we show in Section 5.2 that the effects are negligible. With $\sigma \sim 0$, therefore, equation (33) immediately reduces to the well-known Dyer–Roeder equation,

$$(z + 1)(\Omega_0 z + 1)\frac{\mathrm{d}^2 D}{\mathrm{d}z^2} + \left(\frac{7}{2}\Omega_0 z + \frac{\Omega_0}{2} + 3\right)\frac{\mathrm{d}D}{\mathrm{d}z} + \frac{3}{2}\bar{\alpha}\Omega_0 D = 0, \tag{34}$$

which can be solved analytically for $\Omega_0 = 1$, $\lambda_0 = 0$, and arbitrary $\bar{\alpha}$.

4.2 Generalization of the Dyer–Roeder equation

Starting from the generalized beam equation, quoted by Linder (1998a, b), we have generalized the form of the Dyer–Roeder equation to apply to all the cosmologies we have simulated. This was necessary because solutions for the angular diameter distances were required in the LCDM cosmology containing a vacuum energy density. The procedure to generalize the Dyer–Roeder equation is described fully in the appendix, and solutions of the final equation were obtained numerically. Fig. 1 shows the result of solving the generalized equation, with $\bar{\alpha} = 1$, in the different cosmologies, for a source redshift of $z_s = 3.6$, and Fig. 2 shows the values of the angular diameter distance multiplying
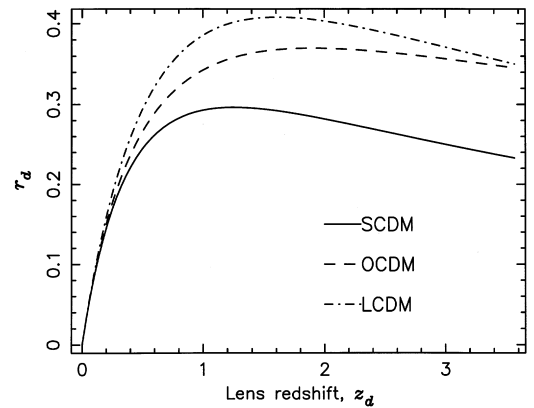

Figure 1. The angular diameter distance, r_d, for three of the cosmologies used here (see Table 1), assuming a source redshift of $z_s = 3.6$, and $\bar{\alpha} = 1$. The maxima of the curves occur at redshifts of 1.24 (SCDM), 1.88 (OCDM) and 1.61 (LCDM).
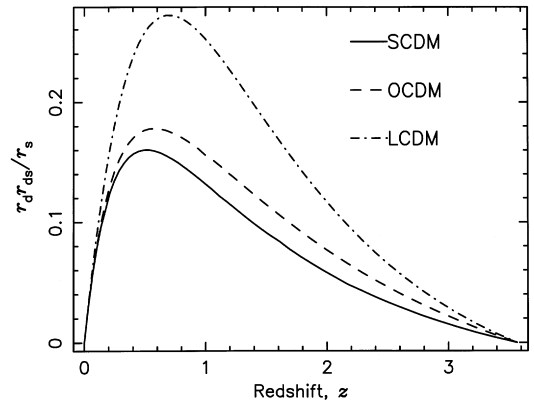

Figure 2. The angular diameter distance multiplying factor, $r_d r_{ds}/r_s$, in three of the cosmologies used here (see Table 1), assuming a source redshift of $z_s = 3.6$, and $\bar{\alpha} = 1$. The maxima of the curves occur at redshifts of 0.53 (SCDM), 0.58 (OCDM) and 0.67 (LCDM).

Table 2. The minimum values of $\bar{\alpha}$, discussed in Section 5.2, which occur at $z = 0$, and the ratios of the R factors at the peaks of the curves in the different cosmologies, assuming a source redshift of 3.6.

Cosmology	Minimum $\bar{\alpha}$	$R(\bar{\alpha} = 1)/R(\bar{\alpha} = 0)$
SCDM	0.83	1.0408
TCDM	0.88	1.0204
OCDM	0.80	1.0241
LCDM	0.82	1.0414

factor, $r_d r_{ds}/r_s$ (which we now denote by R), also for $\bar{\alpha} = 1$. It is clear from this plot that the angular diameter distance multiplying factor is considerably higher in the LCDM cosmology than the other cosmologies, and we shall comment further on this in regard to the weak lensing statistics in the discussion of our results in Section 7. When $\bar{\alpha} = 0$, the values are lower than for $\bar{\alpha} = 1$; we have tabulated the ratios $R(\bar{\alpha} = 1)/R(\bar{\alpha} = 0)$ for the different cosmologies in Table 2.

4.3 Magnification in inhomogeneous universes

Later, in Section 7, we make comparisons of our results with those of other workers, who may use either the full-beam or empty-beam approaches for the propagation of light. We find it difficult to make meaningful comparisons with results obtained using the empty-beam approach, because the magnification distributions, for example, may be quite different, depending on the approach used. We therefore now consider the effects of inhomogeneities, in the different approaches, which are described loosely in terms of Dyer & Roeder's smoothness parameter, $\bar{\alpha}$. We follow the line of reasoning given by Schneider et al. (1992).

Consider our inhomogeneous universe to be on average, i.e., on large scales, homogeneous and isotropic, so that the average flux from a source at redshift z and luminosity L will equal the flux, S_{FL}, observed in a smooth Friedmann–Lemaître universe without local inhomogeneities:

$$\langle S \rangle = S_{FL} = \frac{L}{4\pi[\bar{D}_L(z)]^2}. \tag{35}$$

$\bar{D}_L(z)$ is the luminosity distance in the smooth Friedmann–Lemaître model, and is the mean of the luminosity distance values in an inhomogeneous universe including the constraints of flux conservation. Thus $\bar{D}_L(z)$ can be related to the Dyer–Roeder angular diameter distance, D_s, in an entirely smooth universe (with $\bar{\alpha} = 1$):

$$\bar{D}_L(z) = (1 + z)^2 D_s(z; \bar{\alpha} = 1). \tag{36}$$

Now the magnification, μ, is just the ratio of the flux actually observed in the image of a source and the flux which the same source would produce if observed either through a completely smooth cone or through an empty cone without deflection. Then equation (35) straightaway gives, for the mean magnification in terms of the appropriate Dyer–Roeder angular diameter distances,

$$\langle \mu \rangle = \left[\frac{D_s(z; \bar{\alpha})}{D_s(z; \bar{\alpha} = 1)} \right]^2. \tag{37}$$

Clearly, the magnification values derived in this way depend on the approximation used, and specifically the value of $\bar{\alpha}$. For example, rays passing close to clumps or through high-density

regions will result in magnification in any approximation. If the empty-cone approximation is used, then μ will be greater than 1, and if the full-cone approximation is used, then μ will be greater than the mean magnification. From equation (37) it follows immediately that the mean magnifications, $\langle \mu_e \rangle$ and $\langle \mu_f \rangle$, in the empty-cone and full-beam approximations respectively are

$$\langle \mu_e \rangle = \left[\frac{D_s(z; \bar{\alpha} = 0)}{D_s(z; \bar{\alpha} = 1)} \right]^2 \tag{38}$$

and

$$\langle \mu_f \rangle = 1. \tag{39}$$

$\langle \mu_e \rangle \geq 1$ because $D_s(z; \bar{\alpha} = 0) \geq D_s(z; \bar{\alpha} = 1)$ at all redshifts in all of our cosmologies. This is an important result for advocates of the empty-beam approximation, particularly those working with distributions of point mass particles, because by evaluating numerically the angular diameter distance factors in the different cosmologies (see Appendix A), it immediately follows that

$$\langle \mu_e \rangle(\text{OCDM}) \leq \langle \mu_e \rangle(\text{LCDM}) \leq \langle \mu_e \rangle(\text{SCDM}). \tag{40}$$

Pei (1993) succeeded in calculating the statistical properties of the magnifications due to a random distribution of point mass lenses using the assumption that the total magnification is a result of multiplication of the magnifications produced at each redshift interval. He found that the mean magnification as a function of redshift was exponential in terms of the optical depth, $\tau(z)$:

$$\langle \mu_e(z) \rangle = \exp[2\tau(z)]. \tag{41}$$

[The optical depth is the fraction of the sky covered by circles of Einstein radii between the observer and the specified redshift, and is therefore dependent on the cosmology or the distribution and density of matter. Pei (1993) gives an expression for the optical depth at redshift z in terms of the Dyer–Roeder smoothness parameter and the cosmological density parameter for the point mass lenses in the SCDM cosmology.] Although these are useful results, interpretation of the magnification distributions in the empty-cone approximation for different cosmologies is often complicated by the high-magnification tails in the distributions which arise from light rays passing close to point mass particles. Rauch (1991) set up a random distribution of point masses and performed Monte Carlo simulations to calculate the resulting amplification probability distributions. He then fitted the distribution by an analytical expression for the probability which was given only in terms of the mean magnification. Thus, for a given mean magnification, the distribution curves would be identical, and almost certainly somewhat unrealistic. However, since the mean magnification for sources at a given redshift is dependent on the cosmology, the actual distribution curves are able, in principle, to distinguish between cosmologies.

The minimum magnification in the empty-cone approximation is

$$\mu_{e,\min} = 1. \tag{42}$$

Thus rays passing through voids will have $\mu = \mu_{e,\min} = 1$ in the empty-cone approximation, since the rays will be far from all concentrations of matter, and will satisfy the empty-cone conditions.

In the full-cone approximation however, the magnification for rays passing through voids will be less than or equal to 1, because the rays will suffer divergence, and the minimum value will be

$$\mu_{f,\min} = \left[\frac{D(z; \bar{\alpha} = 1)}{D(z; \bar{\alpha} = 0)} \right]^2 \leq 1. \tag{43}$$
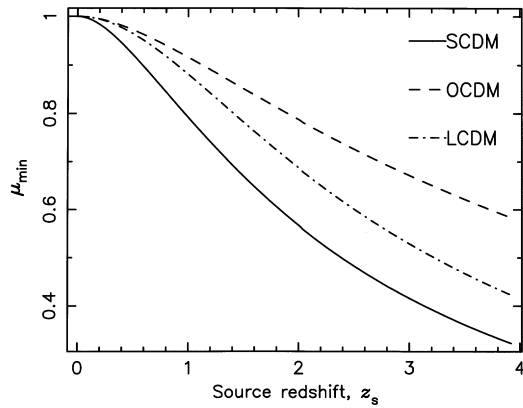
Figure 3. The minimum magnification values versus source redshift for the filled-beam approximation in three different cosmologies.

Table 3. The analytical minimum magnification values in the filled-beam approximation for the different cosmologies, and the computed values from the simulations. It is necessary only that the computed values should be larger than the minima, since the theoretical minima will not, in practice, be seen.

Source redshift	$\mu_{f,min}$ (analytic)	$\mu_{f,min}$ (computed)
SCDM/TCDM		
0.5	0.925	0.955
1.0	0.789	0.903
2.0	0.566	0.833
4.0	0.320	0.749
OCDM		
0.5	0.973	0.980
1.0	0.915	0.951
2.0	0.786	0.889
4.0	0.419	0.792
LCDM		
0.5	0.966	0.977
1.0	0.926	0.879
2.0	0.685	0.825
4.0	0.580	0.715

From this equation, we can again make comparisons amongst our cosmologies. Fig. 3 plots the value of $\mu_{f,min}$ from this equation versus redshift for the different cosmologies, and immediately we can see that

$$\mu_{f,min}(\text{SCDM}) \leq \mu_{f,min}(\text{LCDM}) \leq \mu_{f,min}(\text{OCDM}) \qquad (44)$$

for all redshifts. There are two points to note about this result. First, the minimum magnification values will only rarely (if ever) be seen, because this would require the rays to pass entirely through the most underdense regions. For this reason the values may be treated only as lower bounds for the computed values. Comparisons between the computed minima and these analytic values are shown in Table 3. As required, the computed values are consistently greater than the theoretical minima. Second, the values say nothing about the distribution of magnifications in any cosmology; it is not necessary, for example, for the cosmology producing the lowest minimum magnification to have the broadest range for the probability distribution. Consequently, the results reported in Section 5 require only that the minimum magnifications satisfy the minimum theoretical bounds, and may not relate

in any specific way to results of other workers using point mass particles in an empty-cone scenario. This point is discussed further in Section 7.

5 WEAK LENSING RESULTS IN THE DIFFERENT COSMOLOGIES

5.1 The formation of structure

The formation of structure occurs at different rates in the different cosmologies. Richstone, Loeb & Turner (1992), for example, considered the spherical collapse of density perturbations, starting from an initial Gaussian distribution, and found that the rate of cluster formation as a function of redshift depended crucially on the value of Ω_0. This has been confirmed by, for example, Bartelmann, Ehlers & Schneider (1993). Lacey & Cole (1993), starting from the basic Press-Schechter formulæ, derived an equation for the merger rates of virialized haloes in hierarchical models, which again showed the rates to be crucially dependent on Ω_0. Later, Lacey & Cole (1994) compared their analytical results with the merger rates seen in *N*-body particle simulations for the SCDM cosmology, and found good agreement for this cosmology. In addition, their analytical result was applicable to arbitrary values of Ω_0, and more general power spectra.

Peebles (1993) summarizes the evolution of structure in the Press-Schechter approximation, which provides the number density for collapsed objects by mass scale. This can be evaluated in terms of the rms mass fluctuation, σ_r, at a fixed comoving scale, and so is redshift dependent. For Ω_0 close to 1, $\sigma_r \propto (1+z)^{-1}$, and determines the evolution of the comoving number density of clusters. On this model, half of the present-day clusters would have formed later than $z \sim 0.1$, and 90 per cent would have formed later than $z \sim 0.3$. This rapid evolution at late times in an Einstein–de Sitter universe is seen also in *N*-body simulations. In low-density universes the time evolution of σ_r is slower at low redshift, and this reduces the predicted rate of cluster formation at late times. The Press-Schechter approximation also underestimates the final number density for clusters. Carroll, Press & Turner (1992) describe clearly the rôle of the cosmological constant in the rate of structure formation. As Ω_0 is reduced from unity, the rate of growth is suppressed, but somewhat less so in the presence of a cosmological constant. Thus, in the open case, linear growth stops when $(1+z) \sim \Omega_0^{-1}$, when the universe effectively becomes curvature-dominated, but growth stops more recently, when $(1+z) \sim \Omega_0^{-\frac{1}{3}}$, in the flat case, when the universe effectively becomes dominated by the cosmological constant.

There are clear qualitative differences between Einstein–de Sitter universes and open models from *N*-body simulations. There is much more dominance of clusters and groups of galaxies at earlier times in the open models, which are then frozen in; however, open universes do not display so prominently the large-scale filaments and other irregular structures which occur in $\Omega_0 = 1$ universes. Flat cosmologies with a cosmological constant are intermediate between these cases. It should be mentioned at this point that the results of *N*-body simulations require normalization against observations; whilst the foregoing description of structure formation rates is not very sensitive to the shape parameter, Γ, in the power spectrum, both Γ and the form of the initial conditions (for example, Gaussian or non-Gaussian) may affect the resulting abundances on different scales. For example, the SCDM model fails to reproduce correctly the shape of the
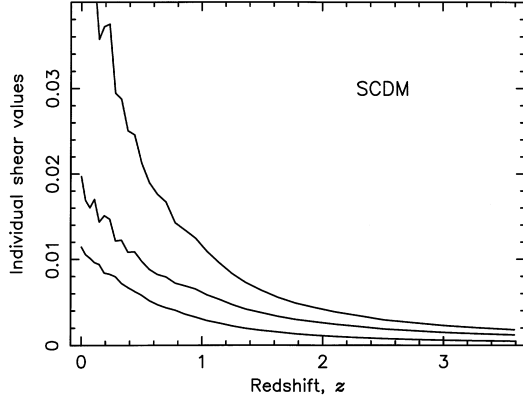
Figure 4. Curves characterizing the time-slices in the SCDM cosmology, derived directly from the computed values, and before applying any of the conversion factors. The ordinate is in arbitrary units. Middle curve: the rms value in each time-slice of the sum of the first two diagonal elements of the shear matrix. Top curve: the mean of the high values of these elements. Bottom curve: the mean of the high values for one of the off-diagonal elements.
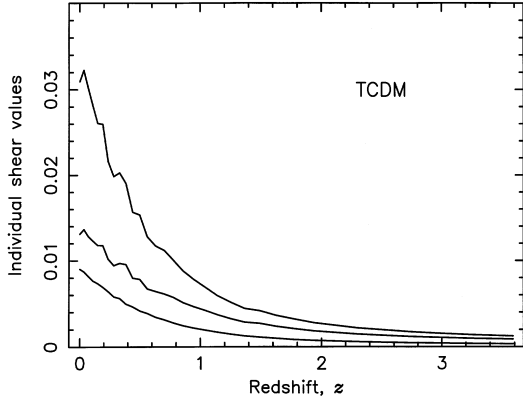

Figure 6. Curves, as for Fig. 4, characterizing the time-slices in the OCDM cosmology.

Figure 5. Curves, as for Fig. 4, characterizing the time-slices in the TCDM cosmology.
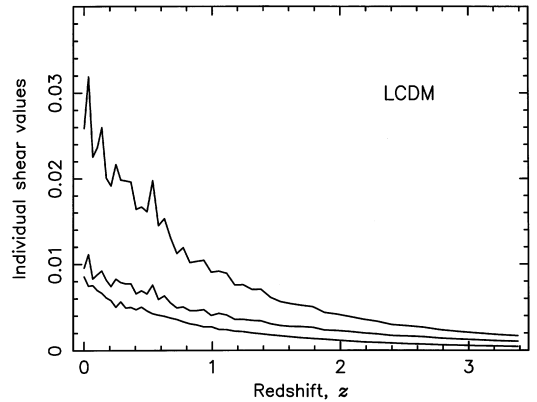
Figure 7. Curves, as for Fig. 4, characterizing the time-slices in the LCDM cosmology.

galaxy correlation function on scales of tens of Mpc, using $\Gamma = 0.5$, but the TCDM model, with $\Gamma = 0.25$ does much better.

We now consider the values of the computed three-dimensional shear in each time-slice, and their development with time, to see whether comparisons may be made with the development of structure in the different cosmologies. It is also informative to assess at what point (or in which simulation boxes) the maximum contributions to properties such as the magnification may occur.

By simply taking the rms values of specified computed components, it is possible, in a simplistic way, to obtain values which characterize each time-slice, independent of its redshift. This is done (a) before integration along the line of sight (which would be necessary to obtain the two-dimensional effective lensing potentials, from which the magnifications are obtained), (b) before conversion to physical units (which involve factors to convert from the code units, and factors which derive from the evolving box dimensions), and (c) before the application of the appropriate angular diameter distance factors (required in the application of the multiple lens-plane theory, described in Section 2). Figs 4–7 show the results for the SCDM, TCDM, OCDM and LCDM cosmologies respectively. In each, the middle

curve shows the rms value in each time-slice of the sum of the first two diagonal elements of the shear matrix, the top curve shows the mean of only the high values of these elements, and the bottom curve shows the mean of the high values for one of the off-diagonal elements. (The high values in each case are those more than 1σ above the mean in the rms values.) The growth in the values with time is clearly seen in each cosmology.

In Fig. 8 we have combined the data for all the different cosmologies. The figure shows the directly computed rms values, as above. The plots can be understood in terms of the discussion at the beginning of this section. The Einstein–de Sitter universes, SCDM and TCDM, show the most rapid growth of the shear components at late times, reflecting the rapid growth of structure; the OCDM and LCDM results would seem to indicate only a limited effect from the cosmological constant.

Since the real physical dimensions of the simulation time-slices evolve with time, it is necessary to introduce factors of $(1 + z)^3$ to the computed values to determine the real shear matrix. Doing this appears to dilute considerably the effect of structure on the form of the curves, as the example of Fig. 9 for the TCDM cosmology shows. (The curves are similar in form for all the cosmologies.) The interpretation of this dilution is that, even though structure is forming (to produce greater shear values locally), the real expansion of the universe (causing the mean particle separation to increase) reduces the shear values in most locations, and therefore just outweighs the increases from the formation of
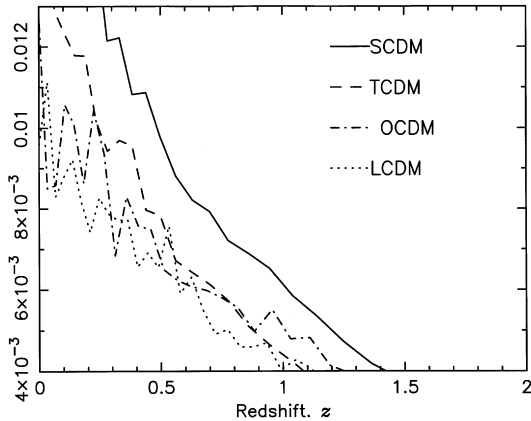
Figure 8. Curves characterizing the time-slices in all the cosmologies, derived directly from the computed values, and before applying any of the conversion factors. The ordinate is in arbitrary units. The curves derive from the rms values in each time-slice of the sum of the first two diagonal elements of the shear matrix.
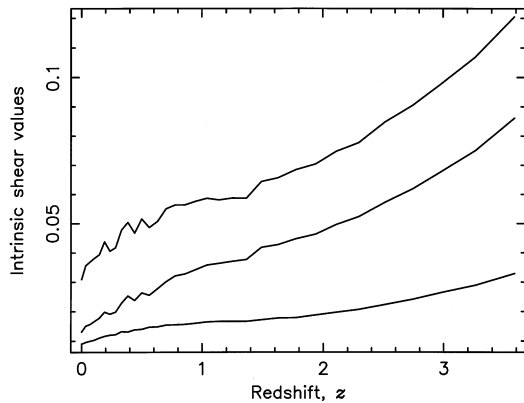

Figure 9. Curves characterizing the time-slices in the TCDM cosmology, obtained by multiplying the computed values by $(1 + z)^3$ in each time-slice. Middle curve: the rms value in each time-slice of the sum of the first two diagonal elements of the shear matrix. Top curve: the mean of the high values of these elements. Bottom curve: the mean of the high values for one of the off-diagonal elements.

structure. In this way, the magnitudes of the shear component values are seen to reduce slowly with time.

To obtain the two-dimensional effective lensing potentials (to which the multiple lens-plane theory may be applied) it is necessary to integrate the three-dimensional values, correctly converted to physical units, along the line of sight, and to apply the appropriate angular diameter distance factors in accordance with equation (23). This requires the integrated three-dimensional computed values (before any of the above factors are applied) to be multiplied by the factor $B(1 + z)^2 r_d r_{ds}/r_s$, where $B = (c/H_0)(2/c^2)GM_{part} \times$ (comoving box depth)$^{-2}$, as described in Section 3.4. When the computed values are multiplied by the full conversion factors in this way, we see in Fig. 10 (for the SCDM cosmology, and a source redshift of 3.9) that the peaks are extremely broad, indicating that significant contributions to the magnifications and ellipticities can arise in time-slices covering a wide range of redshifts, and not just near $z = 0.5$, where the angular diameter distance multiplying factor, R, has its peak (for sources at $z_s = 4$). (In this exercise, we have used $\bar{\alpha} = 1$ for the
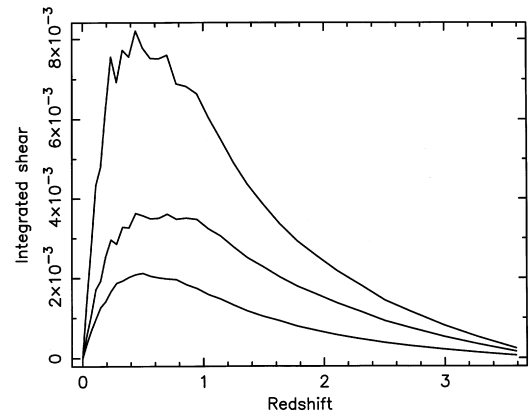

Figure 10. The two-dimensional components in each time-slice in the SCDM cosmology (obtained by integration of the three-dimensional values), converted to absolute values, including the angular diameter distance factors, for sources at $z_s = 3.9$. Middle curve: the rms value in each time-slice of the sum of the diagonal elements of the Jacobian matrix. Top curve: the mean of the high values of the summed diagonal elements. Bottom curve: the mean of the high values for one of the off-diagonal elements of the Jacobian.
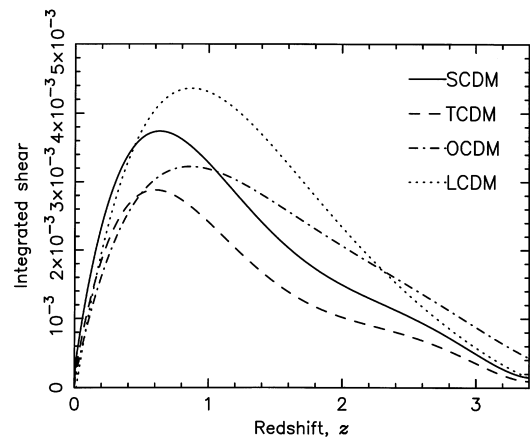

Figure 11. Smoothed rms values of the sum of the diagonal elements of the Jacobian matrix in each time-slice (obtained by integration of the three-dimensional values), converted to absolute values including the angular diameter distance factors, for sources at $z_s = 4$. Results are shown for the SCDM, TCDM, OCDM, and LCDM cosmologies. (The peaks of the curves occur at redshifts of 0.63, 0.60, 0.86 and 0.87 respectively.)

angular diameter distances. This is explained more fully in the next section.)

The comparisons amongst the cosmologies are interesting. Fig. 11 shows the integrated rms values (as above) multiplied by the full conversion factors and the angular diameter distance factors for the four cosmologies, assuming a source redshift of 4. (We have smoothed the curves to emphasize more clearly the widths of the curves and the positions of the peaks, which are quantified in the figure caption; the actual source redshifts differ very slightly in the different cosmologies.) We see that the LCDM cosmology has a very broad peak at the highest values, suggesting that lenses throughout a broad redshift range are able to contribute significantly to magnifications and two-dimensional shearing of images in this cosmology. Because of this, the magnitudes of the magnifications are likely to be greatest in the LCDM cosmology. Significantly, the much higher values for the angular diameter

distance factor, R, in the LCDM cosmology appear to be the more important factor, rather than the existence of structure. The OCDM cosmology also has a very broad peak. The TCDM cosmology has both the narrowest range and the lowest peak. The differences between the SCDM and TCDM cosmologies probably reflect the differences in structure on different scales in the two cosmologies, since R is the same for both. In general, however, we can say that, for all these cosmologies, significant contributions to the magnification and shear may arise from lenses at a very wide range of redshifts.

In a similar study, Premadi et al. (1998a) find that the individual contribution due to each of their lens-planes is greatest at intermediate redshifts, of order $z = 1$–2, for sources located at $z_s = 5$, and Premadi, Martel & Matzner (1998b, 1999) also find very broad peaks covering a wide range of intermediate lens-plane redshifts for sources at $z_s = 3$.

5.2 Results in the different cosmologies

In Section 5.1 we assumed a value of $\bar{\alpha} = 1$ in the determination of the angular diameter distances in the various cosmologies. From the output of the shear algorithm one is able to obtain an estimate of the clumpiness or smoothness in each time-slice. Having set the minimum softening scale, the code declares the number of particles which are assigned the minimum softening, and one can therefore immediately obtain the mass fraction contained in clumps, which we choose to be defined by the minimum softening scale.

For the SCDM cosmology, there is a mass fraction of 0.026 in clumps in the earliest time-slice at $z = 3.6$ (next to $z = 3.9$) giving $\bar{\alpha}(z = 3.6) = 0.97$, and at $z = 0$ the fraction is 0.17, giving $\bar{\alpha}(z = 0) = 0.83$. It is clear that the mean value throughout the redshift range is close to 1, and almost equivalent to the 'filled-beam' approximation. (This result is in agreement with Tomita 1998c, who finds $\bar{\alpha}$ to be close to 1 in all cases.) The multiplying factors, $r_d r_{ds}/r_s$, are very close for the values $\bar{\alpha} = 0.83$ and 1.0, although somewhat different from the values for $\bar{\alpha} = 0$ appropriate for an entirely clumpy universe. The fractional discrepancy between $\bar{\alpha} = 0.83$ and $\bar{\alpha} = 1.0$ at the peak of the curves for the SCDM and TCDM cosmologies is 5.2 per cent for a source at $z_s = 4$, 2.4 per cent for $z_s = 2$, and for sources nearer than $z_s = 1$ the discrepancy is well below 1 per cent.

In the TCDM cosmology with shape parameter 0.25, $\bar{\alpha}$ falls to 0.88 at $z = 0$. The higher value in the TCDM model confirms that the SCDM cosmology (with shape parameter 0.5) has more clumpiness at late times, allowing higher values of magnification and shear to occur. The other cosmologies also have high (though somewhat similar) values for the smoothness parameter at $z = 0$. The values are 0.80 in the OCDM cosmology, and 0.82 in the LCDM cosmology. Table 2 contains the values of $\bar{\alpha}(z = 0)$, which therefore represent the *minimum* values for $\bar{\alpha}$, and also the ratios $R(\bar{\alpha} = 1)/R[\bar{\alpha}(z = 0)]$ at the peaks of the curves for the different cosmologies. These have all been evaluated for a source redshift of 3.6 to enable direct comparisons to be made.

It has been shown by Barber, Thomas & Couchman (1999) that the weak lensing statistics show only a small sensitivity to the smoothness parameter, $\bar{\alpha}$, for values between 0.83 and 1 in the SCDM cosmology. Furthermore, the minimum values in all the cosmologies were always at least 0.8 throughout the redshift range, so that the real values are likely to be closer to unity in every case. We have therefore chosen to present our results on the

basis of $\bar{\alpha} = 1$ throughout for all the cosmologies. This conclusion is validated qualitatively, since the variable softening scheme used in the algorithm ensures that almost all rays pass entirely through softened mass.

The source redshifts, z_s, we have chosen throughout this work are close to 4, 3, 2, 1 and 0.5, and we shall refer to the sources in these terms. The actual redshift values vary slightly for the different cosmologies and appear in Table 4.

We show in Fig. 12 an example of the distributions of the magnifications, μ, in the LCDM cosmology for four different source redshifts. For all the source redshifts and all the cosmologies, there is a significant range of magnification as indicated in Table 4. From these distributions we have computed the values at the peaks, μ_{peak}. Then, since the distributions are

Table 4. Various magnification statistics for the different cosmologies, as described in the text (Section 5.2). The interval from μ_{low} to μ_{high} contains 95 per cent of all the values.

| z_s	μ_{low}	μ_{peak}	rms deviation	μ_{high}
SCDM				
3.9	0.835	0.933	0.115	1.420
3.0	0.852	0.949	0.101	1.367
1.9	0.885	0.947	0.079	1.277
1.0	0.930	0.973	0.049	1.181
0.5	0.969	0.985	0.023	1.089
TCDM				
3.9	0.861	0.959	0.091	1.315
3.0	0.877	0.951	0.081	1.286
1.9	0.904	0.966	0.064	1.228
1.0	0.941	0.972	0.039	1.144
0.5	0.974	0.986	0.019	1.067
OCDM				
4.0	0.858	0.919	0.115	1.469
2.9	0.885	0.939	0.093	1.388
2.0	0.915	0.942	0.069	1.283
1.0	0.960	0.972	0.033	1.147
0.5	0.985	0.989	0.013	1.062
LCDM				
3.6	0.789	0.885	0.191	1.850
2.0	0.870	0.934	0.108	1.453
1.0	0.944	0.966	0.045	1.191
0.5	0.981	0.987	0.016	1.070
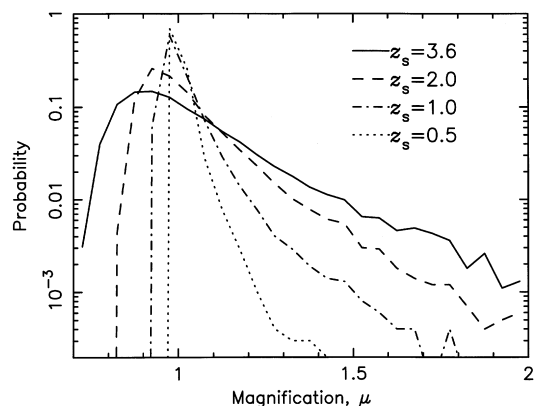
Figure 12. Probability distributions for the magnification, for $z_s = 3.6$, 2.0, 1.0 and 0.5 in the LCDM cosmology.
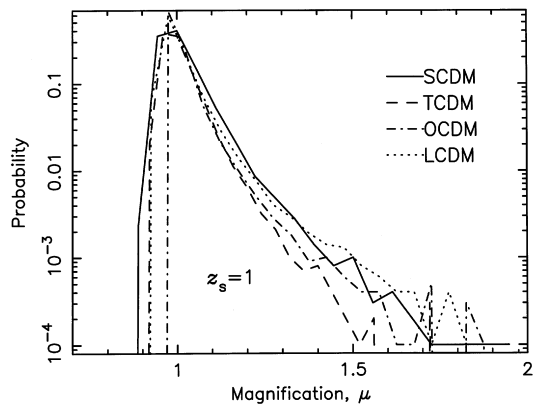
Figure 13. The magnification probability distributions for all the cosmologies, assuming $z_s = 1$.
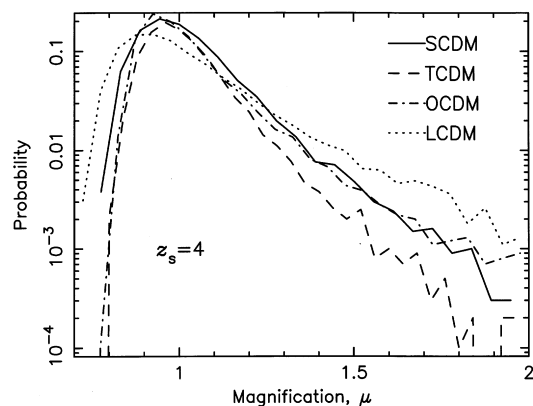

Figure 14. The magnification probability distributions for all the cosmologies, assuming $z_s = 4$.

Figure 15. The probability for which the magnification is greater than the abscissa value. The plot shows the data for all the cosmologies for $z_s = 1$.

Figure 16. The probability for which the magnification is greater than the abscissa value. The plot shows the data for all the cosmologies for $z_s = 4$.

asymmetrical, we have calculated the values, μ_{low} and μ_{high}, above and below which 97.5 per cent of all lines of sight fall, and also the rms deviations from unity for the magnifications. (These latter rms values have been computed only for the lines of sight displaying magnifications between μ_{low} and μ_{high} because three high-magnification events in the LCDM cosmology would distort the rms values considerably.) All the values mentioned are displayed in Table 4.

It is interesting to compare the distributions in the different cosmologies. Figs 13 and 14 show the magnification distributions for all the cosmologies for source redshifts of 1 and 4 respectively. The distributions for the magnifications (and also the convergence, shear and ellipticities) are all broader in the SCDM cosmology when compared with the TCDM cosmology, due to its more clumpy character. For source redshifts of 4 the OCDM and SCDM cosmologies have very similar distributions, even though the angular diameter distance multiplying factors are larger in the OCDM cosmology. For high source redshifts the magnification distributions are broadest in the LCDM cosmology (and the maximum values of the magnification are greatest here), but for lower source redshifts the width of the distribution is below the SCDM and OCDM cosmologies.

We plot in Figs 15 and 16 the probabilities for which the magnifications are greater than the abscissa values (the integrated probabilities). This is done for all the cosmologies for source redshifts of 1 and 4 respectively, and clearly shows the distinctions at the high-magnification end. In particular, the LCDM cosmology
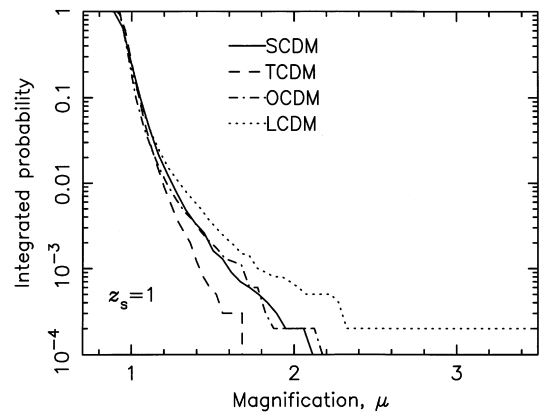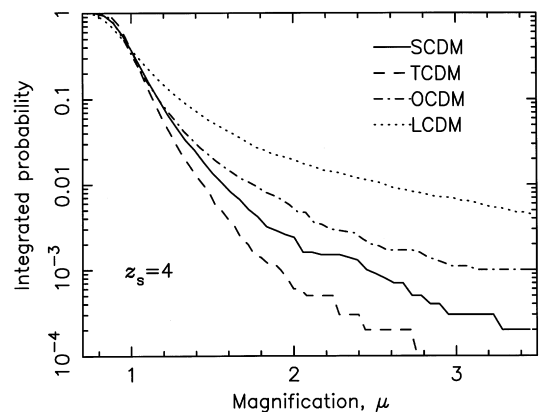
exhibits a very broad tail for $z_s = 4$, and for this reason we show the integrated magnification probability for this cosmology in Fig. 17 for source redshifts of 3.6, 2.0, 1.0 and 0.5.

In Fig. 18 we show the magnification, μ, plotted against the convergence, κ, for $z_s = 4$, again for the LCDM cosmology. Departures from the curve represented by the values of $1/(1 - \kappa)^2$ clearly arise as a result of the presence of the term $-\gamma^2$ in the denominator of equation (28), and are most pronounced at the high-κ end, as might be expected. This is true for all the source redshifts and all the cosmologies.

We would generally expect the shear, γ, to fluctuate strongly for light rays passing through regions of high density (high convergence), and we indeed find considerable scatter in the shear when plotted against the convergence. This would result in different magnification values along lines of sight for which the convergence values are the same. Fig. 19 (reproduced from Barber et al. 1999) shows the result of binning the convergence values in the SCDM cosmology and calculating the average shear in each bin, for sources at $z_s = 4$. We see that throughout most of the range in κ the average shear increases very slowly, and closely linearly, and we have found similar trends in the other cosmologies. (At the high κ-end there are too few data points to establish accurate average values for γ.) This result suggests that there may be a trend towards higher mean magnification values (as κ increases) than would be the case if $\langle\gamma\rangle$ were constant.

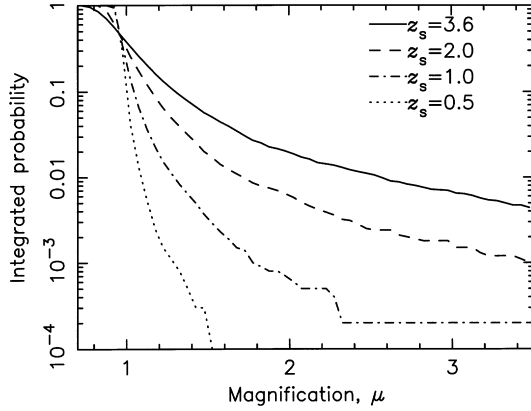Figs 20 and 21 show the distributions in the convergence, κ,

Figure 17. The probability for which the magnification is greater than the abscissa value. The plot shows the data for the LCDM cosmology for four different source redshifts as indicated.
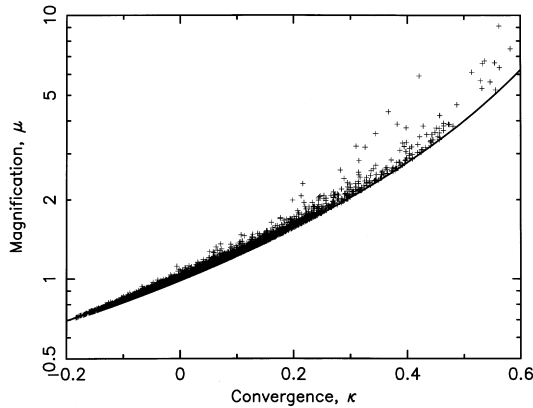

Figure 18. LCDM cosmology: μ versus κ for $z_s = 4$ (crosses). The continuous line, shown for comparison, represents $\mu = 1/(1 - \kappa)^2$.
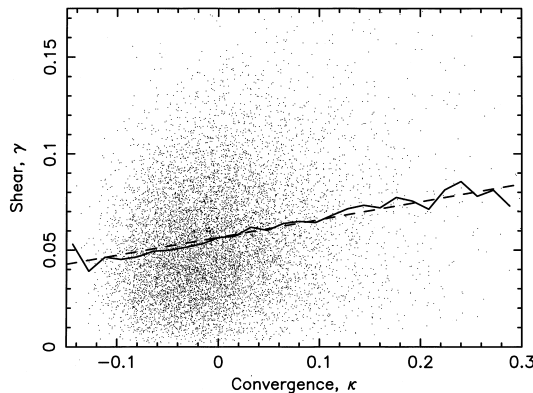

Figure 19. SCDM cosmology: Shear versus convergence for sources at $z_s = 4$ (dots), and the average shear (full line) in each of the κ bins. The plot shows a slow and nearly linear increase with increasing convergence, as indicated by the (dashed) straight line. (The plot has been reproduced from Barber et al. 1999.)

primarily responsible for the magnifications for all the cosmologies, for $z_s = 1$ and $z_s = 4$ respectively.

Table 5 shows the rms values for κ in the different cosmologies for all the source redshifts, and compares them with the rms values for the magnifications. (This time, unlike Table 4, the rms values have been computed from all lines of sight, rather than just those
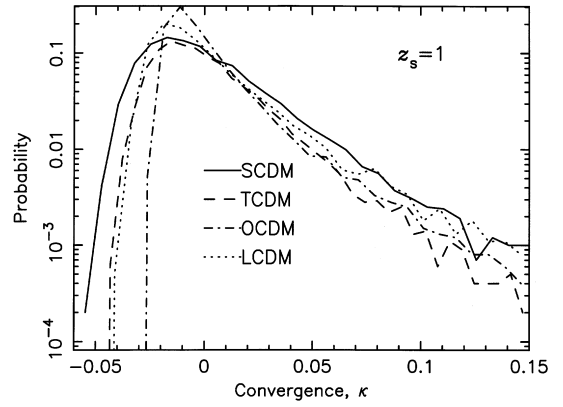

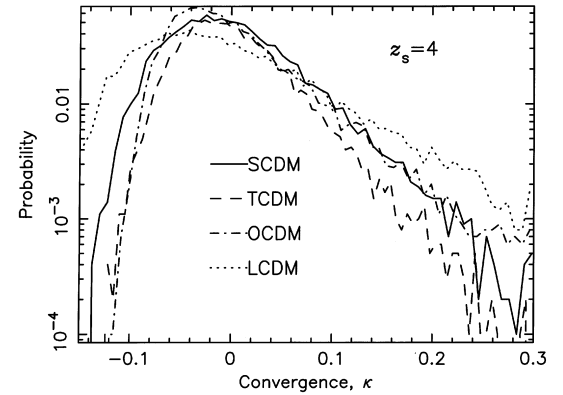**Figure 20.** The probability distributions for the convergence in the different cosmologies, assuming $z_s = 1$.

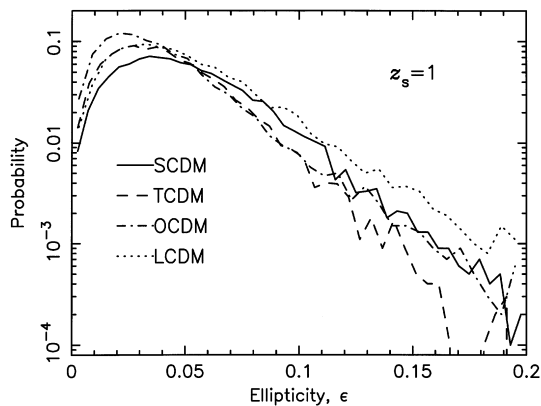**Figure 21.** The probability distributions for the convergence in the different cosmologies, assuming $z_s = 4$.

with magnifications between μ_{low} and μ_{high}. We have not included the values for source redshifts of $z_s = 3.6$ in the LCDM cosmology where some strong lensing events were evident, including two events with negative magnifications indicative of the production of multiple images.)

The distributions in the shear, γ (defined according to equation 26) are broadest, as expected, for the highest source redshifts, and, as before, the LCDM cosmology displays the broadest distribution for γ for sources at high redshift.

The ellipticity, ϵ, in the image of a source is primarily produced by the shear, and we show in Fig. 22 the probability distributions for ϵ for $z_s = 1$ for all the cosmologies. Fig. 23 shows the integrated probability for which the ellipticity is greater than the abscissa value, again for $z_s = 1$ and for all the cosmologies. Figs 24 and 25 show the same information for $z_s = 4$. From the integrated distributions, 90 per cent of all lines of sight have ellipticities greater than 0.016 (SCDM), 0.013 (TCDM), 0.009 (OCDM) and 0.015 (LCDM) for sources at $z_s = 1$. The corresponding figures for $z_s = 4$ are 0.034 (SCDM), 0.027 (TCDM), 0.033 (OCDM) and 0.057 (LCDM). Although the distributions in Figs 22 and 24 are a little noisy, the peaks in the distributions are seen to occur around $\epsilon = 0.034$ (SCDM), 0.027 (TCDM), 0.021 (OCDM) and 0.033 (LCDM) for $z_s = 1$, and around $\epsilon = 0.075$ (SCDM), 0.057 (TCDM), 0.081 (OCDM) and 0.111 (LCDM) for $z_s = 4$. Once again, we see that the LCDM cosmology produces the greatest variation and the highest peak values at high redshift, although this is not the case for sources at lower redshifts.

Table 5. The rms deviations in the magnification and convergence for the different cosmologies.

z_s	Magnification rms deviation	Convergence rms deviation
SCDM		
3.9	0.171	0.064
3.0	0.149	0.058
1.9	0.115	0.047
1.0	0.073	0.031
0.5	0.037	0.016
TCDM		
3.9	0.126	0.052
3.0	0.111	0.047
1.9	0.088	0.038
1.0	0.056	0.025
0.5	0.027	0.013
OCDM		
4.0	0.245	0.066
2.9	0.176	0.056
2.0	0.123	0.044
1.0	0.060	0.024
0.5	0.026	0.012
LCDM		
3.6	N/A	N/A
2.0	0.314	0.064
1.0	0.120	0.032
0.5	0.030	0.013

Figure 22. The probability distributions for the ellipticity for all the cosmologies, for $z_s = 1$.

The ellipticity is very closely linear in terms of γ throughout most of the range in γ, for all the cosmologies. Some scatter occurs because of the factor containing the convergence, κ, in equation (30).

Finally, the distance–redshift relation, equation (33), implies that there may be an effect on the angular diameter distances from the shear. Barber et al. (1999) investigated this for the SCDM cosmology, and found that whilst the maximum effects of shear on the mean magnification values may be at least 10 per cent, only 3.2 per cent of the lines of sight were affected in this way. Also, they pointed out that the shear has an effect in the distance–redshift relation equivalent to increasing the effective smoothness parameter, $\bar{\alpha}$, and this is true for all the cosmologies. By substituting the mean shear value (from the SCDM cosmology) determined for sources at $z_s = 0.5$ (where the term in σ in
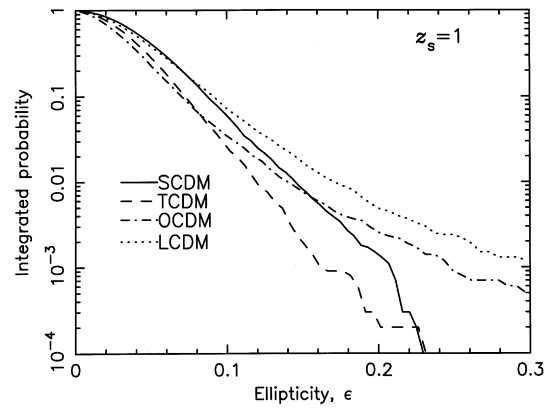
Figure 23. The probability for which the ellipticity is greater than the abscissa value. The plot shows the data for all the cosmologies for $z_s = 1$.
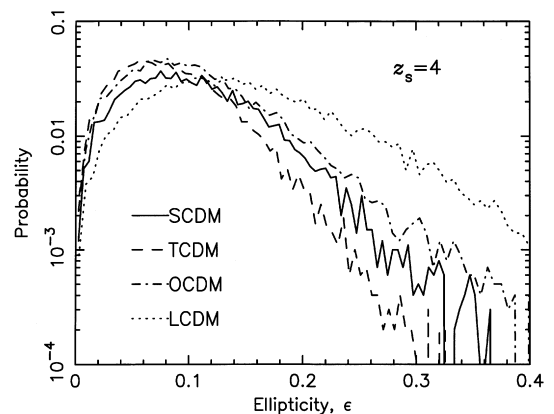
Figure 24. The probability distributions for the ellipticity for all the cosmologies, for $z_s = 4$.

equation 33 is largest), they found the effect on $\bar{\alpha}$ (and therefore on the angular diameter distances) to be completely negligible. Furthermore, the importance of the effect reduces with redshift, so that our decision to ignore the effects of shear in the distance–redshift relation is justified.

6 DETERMINATION OF THE COSMOLOGICAL PARAMETERS

6.1 Weak shear statistics and the density parameter

Jain & Seljak (1997) have given careful consideration to the interpretation of observed shear data (from measured galaxy ellipticities) by comparing with the analytical results of second-order perturbation theory. They claim that non-linear evolution leads to non-Gaussian effects in the weak lensing statistics which are more easily detected in second-order, and higher order, moments. In particular, the probability distribution for the three-dimensional density contrast,

$$\delta(\mathbf{r}) = \frac{\rho(\mathbf{r})}{\bar{\rho}} - 1, \tag{45}$$

is almost indistinguishable in the different cosmologies, whereas the probability distribution function for the convergence, κ, shows different peak amplitudes and different dispersions in the different cosmologies. This is because the transition to non-linearity in the evolution of structure depends primarily on the density contrast
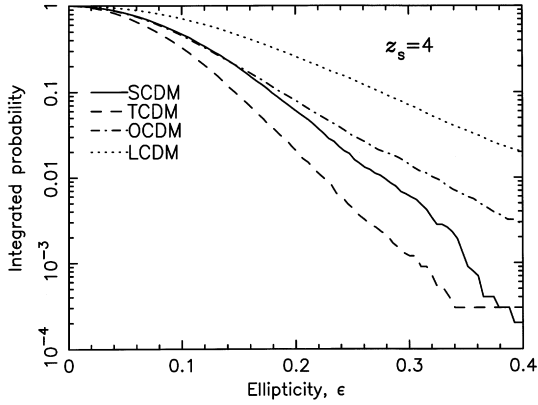
Figure 25. The probability for which the ellipticity is greater than the abscissa value. The plot shows the data for all the cosmologies for $z_s = 4$.
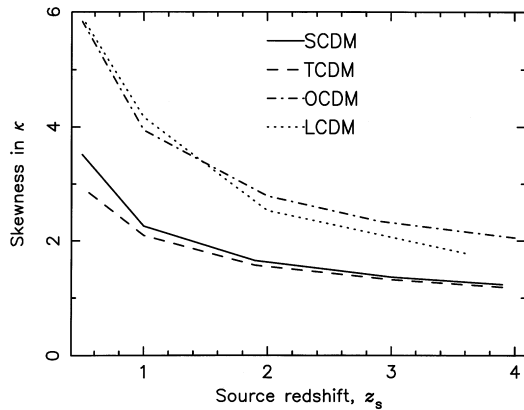

Figure 26. The skewness in κ, according to equation (46), as a function of redshift for the different cosmologies, indicating broadly that the skewness decreases with the density parameter, Ω_0.

alone, but the weak lensing signal is strongest in those cosmologies which have developed structure at optimum redshifts for given source positions, and therefore depends more directly on the rate of evolution. Specifically, the non-linear evolution of the power spectrum introduces non-Gaussianity to the weak lensing statistics, whilst the matter density parameter, Ω_0, (and to some degree the vacuum energy density parameter, λ_0) determines the dispersion in the statistics.

Jain & Seljak (1997) have computed the expected skewness, S, in the convergence,

$$S = \frac{1}{\sigma^3} \langle (\kappa - \bar{\kappa})^3 \rangle, \tag{46}$$

where σ represents the standard deviation in the distribution for κ. As expected, the skewness was greatest on small angular scales, and largest for sources at the lowest redshifts. In general, the LCDM cosmology produced the greatest skewness, followed by the OCDM, and finally the SCDM cosmologies, for sources at low redshift. Even though they have assumed an empty beam scenario with $\bar{\alpha} = 0$, and correspondingly different angular diameter distances from our work, our own results for the skewness in κ are quite consistent with theirs. We have computed the skewness, not on different angular scales, but as a function of redshift for the different cosmologies. It is not possible to state a specific angular scale for our data, because of the variable softening approach in the shear algorithm. Fig. 26 confirms that, at redshifts less than
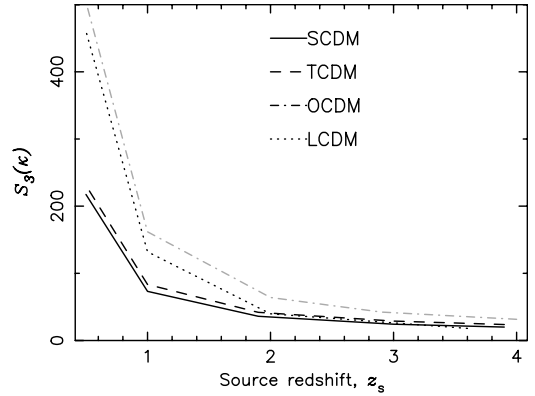
Figure 27. The statistic $S_3(\kappa)$, defined by equation (47), as a function of redshift for the different cosmologies. It is clear that the low-density cosmologies have higher values of S_3 at low redshifts.

about 1.5, the LCDM cosmology gives rise to the largest skewness, followed by the OCDM cosmology, and finally, the SCDM and TCDM cosmologies. The difference between the SCDM and TCDM cosmologies does suggest different forms of structure, which result directly from the input shape parameter, Γ, in the power spectrum. In broad terms, it is clear that the skewness decreases with source redshift, and decreases with the density parameter, precisely as expected from perturbation theory.

Bernardeau, van Waerbeke & Mellier (1997) also use perturbation theory (and the empty-beam approach) to assess how the low-order moments in the convergence may depend on the cosmological parameters. A number of results are predicted. They define the moment, S_3 (*not* the skewness, defined above), by

$$S_3 = \frac{\langle \kappa^3 \rangle}{\langle \kappa^2 \rangle^2}, \tag{47}$$

and predict that $S_3 \propto \Omega_0^{-0.8}$ for $z_s \sim 1$, or $S_3 \propto \Omega_0^{-1.0}$ for $z_s \ll 1$, and they predict a slightly weaker dependence on Ω_0 for $z_s > 1$. We do not find these exact relationships because working in the full-beam approximation with variable smoothing alters the predictions. However, we do find that the value of this statistic does decrease with increasing Ω_0. Our results for S_3 are displayed in Fig. 27. Bernardeau et al. predict significantly less dependence on λ_0.

Jain et al. (2000) have used ray-tracing in *N*-body simulations, as described in the introduction, in an attempt to evaluate the density parameter from weak lensing statistics. Since they make use of the empty-beam approximation, they describe the possibility of many more lines of sight passing through voids from $z_s = 1$ in open universes, because of the earlier beginning to structure formation. They suggest that this means that the probability distribution for κ in open universes will have its peak close to the minimum value. Higher density universes will have the peak well away from the minimum, so that the shape of the distribution will be less steep. Moreover, they state that this situation only applies on small scales, and on such scales this points to the minimum value of κ being roughly proportional to Ω_0. A better statistic in the empty-beam approximation would be that $(\langle \kappa \rangle - \kappa_{min}) \propto \Omega_0$. However, they admit that the result 'does depend somewhat on the geometry, as the pathlength and angular scale differ between open and cosmological constant models with the same Ω_0.' More specifically, this result will depend crucially on the approximation used, i.e., the empty- or full-beam approximation, and the procedure for particle smoothing. They find that the
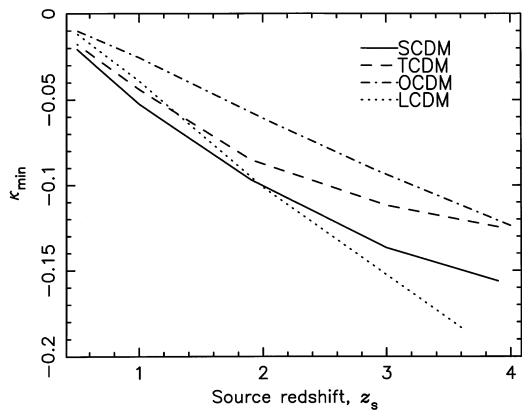
Figure 28. κ_{min} versus redshift for the different cosmologies at low redshift, showing the order expected from the values of Ω_0.
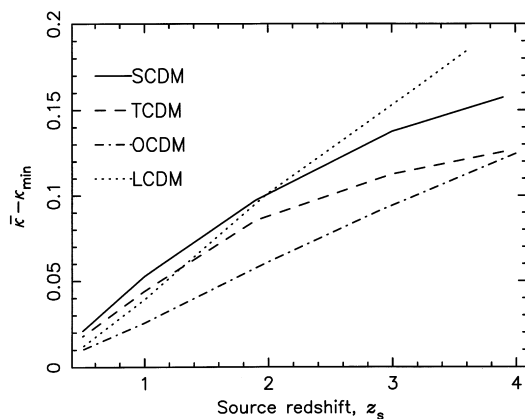

Figure 29. $(\langle\kappa\rangle - \kappa_{min})$ versus redshift for the different cosmologies at low redshift, showing the order expected from the values of Ω_0.

measured minimum for κ in the open cosmology is close to the predicted value, but that in the critical, $\Omega_0 = 1$, cosmology the value was far from the empty-beam value because there were actually no completely empty lines of sight. Our full-beam approach will, of course, represent the extreme case. It is therefore reassuring to see that both our κ_{min} (Fig. 28) and $(\langle\kappa\rangle - \kappa_{min})$ (Fig. 29) values for the different cosmologies are of the order expected from the values of Ω_0. However, because of the entirely different approach from that of Jain et al. (2000), our results are not able to indicate specific values for Ω_0.

Jain et al. (2000) also find for the S_3 statistic that $S_3(OCDM) > S_3(LCDM) > S_3(TCDM) > S_3(SCDM)$ at low redshift. This concurs with our findings (see Fig. 27). They quantify the difference between the SCDM and TCDM cosmologies in terms of a weak function of the shape parameter, which occurs in the expression for S_3 from perturbation theory.

They have also explained in some detail how observational data may be used to reconstruct the convergence, which is only feasible with large fields where the weak shear signal is measurable. However, in view of our quite different approaches, which clearly give rise to discrepancies (although only in terms of degree), care must be taken when interpreting observational data in this way. If we had a better understanding of the form, distribution and evolution of the dark and luminous matter in the Universe, it might be possible to produce simulations and weak lensing experiments in more realistic scenarios.

White & Hu (2000) have undertaken similar work in an LCDM cosmological model with $\sigma_8 = 1.2$ and using both 128^3 and 256^3 particles with a PM code. Their algorithm computes weak lensing statistics, from which they find that the non-Gaussianity of the distributions substantially increases the sampling errors for the skewness and kurtosis of the convergence in the several to tens of arcminutes regime. These sampling errors are, of course, crucial when interpreting observations in terms of cosmological models.

6.2 Weak lensing of high-redshift type Ia supernovae

We have seen in Section 5 the significant ranges in magnifications (dependent on the cosmology) which might apply to distant sources. In the absence of magnification (or demagnification) from the large-scale structure, it would be possible to determine the cosmological parameters, Ω_0 and λ_0, from the departures from linearity in the Hubble diagram, provided 'standard candle' sources together with good calibration were available for measurement at high redshift. This is precisely the route taken by a number of authors, most importantly Riess et al. (1998) and Perlmutter et al. (1999), both of whom have used high-redshift type Ia supernovae data of redshifts up to 0.97. It is evident from our results that full account must be taken of the ranges in magnification for each of the cosmologies, and in particular the cosmologies suggested by the high-redshift type Ia supernovae results.

Both groups of workers, i.e., Riess et al. (1998) and Perlmutter et al. (1999), point to cosmologies which are close to the $\Omega_0 = 0.3$, $\lambda_0 = 0.7$ cosmological simulation we have analysed in terms of weak lensing. Consequently, our results from this cosmology are of considerable interest for their impact on the determination of the cosmological parameters. Using the data we report here, Barber (2000) finds that true underlying cosmologies having a deceleration parameter $q_0 = -0.51 + 0.03/-0.24$ may be interpreted as having $q_0 = -0.55$, from the use of perfect standard candles (without intrinsic dispersion), arising purely from the effects of weak lensing. This significant dispersion in q_0 (approximately 2σ) is somewhat larger than that found by Wambsganss et al. (1997) based on a cosmology with $\Omega_M = 0.4$, $\Omega_\Lambda = 0.6$, because of our broader magnification distribution at $z = 1$.

7   SUMMARY OF RESULTS

In the application of the code for the three-dimensional shear, we have had to consider what appropriate angular diameter distance values should be applied to the data. The values have all been calculated numerically from the generalized beam equations (see Section 4) for the different cosmologies. This was done in each case for a smoothness parameter $\bar{\alpha} = 1$. Our variable softening scheme for the particles ensures that nearly all rays pass entirely through softened mass and, in addition, we found that the minimum value of $\bar{\alpha}$ was at least 0.8 (at $z = 0$) in all the cosmologies. The differences in the magnification distributions for $\bar{\alpha} = 1$ and for the minimum value were almost indistinguishable. The effects of shear on the angular diameter distances (through changes to the effective value of the smoothness parameter, $\bar{\alpha}$), were found to be completely negligible at all redshifts, so we are justified in ignoring them in the distance–redshift relation. Furthermore, they are always additive, making the effective value of $\bar{\alpha}$ even closer to unity.

We found, in Section 5.1, that the Einstein–de Sitter universes showed the most rapid growth in the 'intrinsic' shear components at late times, as expected from the growth of structure in these cosmologies. This was as a result of studying the computed shear values before the application of the angular diameter distance factors, and before conversion to physical units. The OCDM and LCDM cosmologies indicated only a limited contribution from the cosmological constant in terms of the growth in the shear values, again consistent with the expected evolution of structure in these cosmologies.

When the computed shear values were multiplied by the full conversion factors appropriate to the integration, together with the angular diameter distance factors, the resulting curves exhibited very broad peaks, indicating that significant lensing may result from structure in a wide band of redshifts. Significantly, the LCDM cosmology has both the broadest and the highest peak, indicating that this cosmology should produce, for example, the broadest range of magnifications. This result would appear to come primarily from the large values of the angular diameter distance factors for this cosmology, rather than any considerations about the evolution of structure. However, the broader and higher peak for the SCDM cosmology, compared with the TCDM cosmology, does indicate the differences in structure within them, since they both have the same values for the angular diameter multiplying factor, R.

In Section 5.2 we showed the results for the magnification distributions for the different cosmologies for different source redshifts, and these are concisely summarized in Table 4. At high redshift, the LCDM cosmology produces the highest magnifications, the broadest distribution curves, and the lowest peak values. For sources at $z_s = 3.6$ in the LCDM cosmology, 2.5 per cent of all lines of sight have magnification values greater than 1.850. (The maximum magnifications, not quoted here, depend on the choice of the minimum softening in the code, although the overall distributions are very insensitive to the softening.) The rms fluctuations in the magnification (about the mean) were as much as 0.191 in this cosmology, for sources at $z_s = 3.6$. Even for sources at $z_s = 0.5$ there is a measurable range of magnifications in all the cosmologies.

The immediate implication of these results is the likely existence of a bias in observed magnitudes of distant objects, and a likely dispersion for standard candles (for example, type Ia supernovae) at high redshift.

The magnification versus the convergence showed the presence of significant shear, and the mean values of γ in small convergence bins pointed to a possible slow linear increase in $\langle\gamma\rangle$ with κ. This would result in a trend towards higher mean magnification values (as κ increases) than would be the case for constant $\langle\gamma\rangle$.

The distributions for the shear, γ, are broadest, in the LCDM cosmology for high source redshifts, and there are closely linear relationships between the ellipticity and the shear in all the cosmologies. This relationship leads again to broad distributions in the ellipticity for high-redshift sources in the LCDM cosmology. The peak in the ellipticity distribution for the LCDM cosmology, for $z_s = 3.6$, is 0.111, being almost twice the value in the TCDM cosmology.

Jain et al. (2000) have expressed the possibility of determining the value of the density parameter from the convergence field from weak lensing statistics. They show one-point distribution functions for κ, assuming sources at $z_s = 1$, for all their four cosmologies and using different (fixed) smoothing scales in each.

They describe the increasing non-Gaussianity of the distribution functions as the smoothing scale is reduced, and the increasing tail at high κ. They also describe the shape of the distribution functions for negative κ, which results from the rate of structure formation in the different cosmologies, and claim the interesting conclusion that the minimum value of κ is proportional to the density parameter. We were able to establish from our own work that, in broad terms, the skewness in κ decreases with source redshift, and decreases with increasing density parameter, as expected. Also, the statistic S_3 (defined in equation 47) was found to decrease with increasing Ω_0. However, we were unable to establish more precise relationships, because of the use of the full-beam approximation. The order of the cosmologies for S_3 is the same as that presented by Jain et al. (2000). We also found that both κ_{min} and $(\langle\kappa\rangle - \kappa_{min})$ are of the correct order for the different cosmologies in terms of Ω_0, although, again for the same reason, it would not be possible to obtain specific values for Ω_0.

8 COMPARISONS WITH OTHER WORK AND CONCLUSIONS

We now, very briefly, make some comparisons with the weak lensing results obtained by other authors. This will not be exhaustive, because it has been anticipated that our results should be different, for a number of reasons. Primary amongst these are the following. First, our results were obtained using the three-dimensional shear code, which allows periodicity, the use of the peculiar potential, the net zero mean density requirement, and angular diameter distances to every evaluation position within each simulation volume. Second, many two-dimensional (planar) approaches may suffer from inadequate convergence to the true limiting values for the shear matrix and angular deflections. Third, we have introduced a physically realistic variable softening to the method, which requires use of the full-beam approximation for the angular diameter distances, rather than the empty-cone approximation used by many authors with either point masses, small (fixed) softenings, or small pixellation in the planes.

The magnification distributions of Jaroszyński et al. (1990) for the SCDM cosmology do not have mean values of 1, and their dispersions in the convergence for sources at $z_s = 1$ and $z_s = 3$ are considerably lower than our values, with very little evolution with redshift. In our work, the peaks of the ellipticity distributions occurred at values of 0.075 (similar to the value for $z_s = 4$) and 0.034 for sources at $z_s = 3$ and 1 respectively, and these are somewhat lower than the values of 0.095 ($z_s = 3$) and 0.045 ($z_s = 1$) found by Jaroszyński et al. Rather surprisingly, however, their peak values in the distributions for the shear are quite similar to ours, especially for sources at $z_s = 3$.

Wambsganss et al. (1998) find magnifications up to 100 in the SCDM cosmology, and correspondingly highly dispersed distributions, very much larger than ours for $z_s = 3$. The high-magnification tail in the distributions almost certainly derives from the low value of the (fixed) softening scale resulting from the 'smearing' of the mass distribution in the $10\,h^{-1}\,\text{kpc} \times 10\,h^{-1}$ kpc pixels.

Similarly, Marri & Ferrara (1998) show wide magnification distributions, and very high maximum values, which again occur as a result of using point particles rather than smoothed particles. Their procedure (summarized in Section 1.2) is completely different from ours, and, unlike us, they find that the SCDM

cosmology has the broadest magnification probability distribution, followed by the LCDM cosmology, and finally their HCDM cosmology. In particular, we would disagree with their choice of $\bar{\alpha} = 0$, which is representative of an entirely clumpy universe, as opposed to our finding that the SCDM universe is close to being smooth at all epochs.

Hamana et al. (2000) find that the dispersions in the probability distributions for κ, γ and μ are all greatest for the Einstein–de Sitter cosmology, and are very similar for their open and cosmological constant cosmologies. This is in contrast to our findings. In addition, their magnification and convergence distributions for $z_s = 1$, 2 and 3 are much broader than ours. These differences arise most likely because of the different normalizations, σ_8, in their simulations. Surprisingly, however, the widths of the distributions for γ in the SCDM cosmology are similar to ours.

The ranges in magnification from Premadi et al. (1998a) appear to be rather similar to ours for sources at $z_s = 3$ for their three cosmologies, and the widths of the distributions are of the same order for the different cosmologies that we find. This is reassuring because, although their method relies on two-dimensional projections of the simulation boxes, they include many of the essential features to which we have drawn attention, for example, an assumed periodicity in the matter distribution, randomly chosen initial conditions to avoid structure correlations between adjacent simulation boxes, the net zero mean density requirement, realistic mass profiles for the particles, and use of the filled-beam approximation with a smoothness parameter, $\bar{\alpha} = 1$. They show the average shear for a source at $z_s = 5$ contributed by each of the lens-planes individually, and find that the largest contributions come from those planes at intermediate redshift, of order $z = 1$–2. Similarly, they find that the lens-planes which contribute most to the average magnifications are also located at intermediate redshifts. In terms of the development of structure in the different cosmologies, they find that the lens-planes contributing the most shear and magnification are located at larger redshifts for those cosmologies with smaller Ω_M. The average shear for each redshift has been plotted by the authors. They find that the average shear contributed by each lens-plane is many times greater in their Einstein–de Sitter cosmology than in their cosmological constant model for all redshifts, and this in turn is greater than in their open cosmology. This is because the total mass is 5 times greater in their Einstein–de Sitter cosmology, whilst the mass in galaxies is similar for all the cosmologies. However, when the cumulative shear is computed, taking account also of the number of lens-planes in each cosmology, they find that the magnitudes of the shear in the cosmological constant model are significantly larger than the values in the other two cosmologies for sources at $z_s = 5$. We also find this at the higher redshifts.

Fluke et al. (2000), in applying the ray bundle method of Fluke et al. (1999), explain clearly the differences between the empty-cone and full-beam approximations. They use the empty-cone approximation, because of their use of an effective fixed physical radius for each particle, equal to $\sqrt{2} \times$ the Einstein radius for each. This gives rise to magnification probability distributions with $\mu_{min} = 1$, arising from the use of $\bar{\alpha} = 0$, and high-magnification tails, arising from the small effective radii for particles and clusters. They obtain the weak lensing statistics for the same cosmologies we have used. For $z_s = 1$, the distribution in the magnifications for the SCDM cosmology is clearly broader than that for the LCDM cosmology, which in turn is broader than the OCDM cosmology. This is also true of our data, although the

order for the cosmologies, in our work, is completely altered for higher source redshifts. The authors find, as do we, that the most significant differences amongst the cosmologies arise directly as a result of the optical depth to the source, which is related to the angular diameter distances. Moreover, there is a suggestion in their results (Fluke, private communication) that Kolmogorov–Smirnov tests may be unable to distinguish the cosmologies, *even random distributions of particles,* in terms of their magnification distributions, if the same set of angular diameter distance factors is applied to each.

This last statement may prove to be extremely important, as it appears from both our own work and that of Fluke et al. (2000) that the angular diameter distances (or optical depths) are really the determining factor for weak lensing statistics. Moreover, our two approaches may represent 'limits' for the true lensing behaviour from the mass distribution in the Universe. The variable softening facility within our algorithm leads naturally to the assumption that the Universe may be described in terms of the full-beam approximation. This is, however, quite different from the assumptions of many other workers, who frequently use point particles, or a limited form of fixed softening, or small pixellation, and therefore use the empty-beam approximation. The two approaches give rise to quite different expectations and results. The most obvious differences are the following. First, strong lensing can occur with effectively small particles, leading to high-magnification tails in the probability distributions. Second, magnification distributions in the empty-cone approximation all have $\mu_{min} = 1$, whilst in the full-beam approximation, $\mu_{min} \lesssim 1$; this may alter the dispersions in the two distributions. Third, the mean values for the magnifications can be calculated from the respective angular diameter distances in the different cosmologies for the empty-beam approximation; however, the mean values in the full-beam approximation are always 1. These points make comparisons between methods using the different approximations difficult. However, it is probable that the Universe is neither completely smooth nor filled with galactic-mass point-like objects. (Subramanian, Cen & Ostriker 2000 highlight our uncertainty in this area, by suggesting that small dense masses formed early during hierarchical clustering may persist to late times, so that real cluster halo structures may depend crucially on the detailed dynamics of the dense pockets.) The resolution of this question, together with a better understanding of the form, distribution and evolution of the dark and luminous matter content of the Universe, should provide a much clearer indication of the likely weak lensing statistics in cosmological *N*-body simulations of the future.

ACKNOWLEDGMENTS

REFERENCES

Barber A. J., 2000, MNRAS, in press (astro-ph 0003304)
Barber A. J., Thomas P. A., Couchman H. M. P., 1999, MNRAS, 310, 453
Bartelmann M., Ehlers J., Schneider P., 1993, A&A, 280, 351
Bernardeau F., van Waerbeke L., Mellier Y., 1997, A&A, 322, 1

Carroll S. M., Press W. H., Turner E. L., 1992, ARA&A, 30, 499

Couchman H. M. P., Thomas P. A., Pearce F. R., 1995, ApJ, 452, 797

Couchman H. M. P., Barber A. J., Thomas P. A., 1999, MNRAS, 308, 180

Dyer C. C., Roeder R. C., 1973, ApJ, 180, L31

Fluke C. J., Webster R. L., Mortlock D. J., 1999, MNRAS, 306, 567

Fluke C. J., Webster R. L., Mortlock D. J., 2000, MNRAS, submitted

Hamana T., Martel H., Futamase T., 2000, ApJ, 529, 56

Hockney R. W., Eastwood J. W., 1988, Computer Simulation Using Particles. IOP Publishing, ISBN 0-85274-392-0

Jain B., Seljak U., 1997, ApJ, 484, 560

Jain B., Seljak U., White S., 1998, MPA/ESO Cosmology Conference, Garching

Jain B., Seljak U., White S., 2000, ApJ, 530, 547

Jaroszyński M., Park C., Paczynski B., Gott J. R., III, 1990, ApJ, 365, 22

Lacey C., Cole S., 1993, MNRAS, 262, 627

Lacey C., Cole S., 1994, MNRAS, 271, 676

Linder E. V., 1998a, A&A, 206, 175

Linder E. V., 1998b, A&A, 206, 190

Marri S., Ferrara A., 1998, ApJ, 509, 43

Peacock J. A., Dodds S. J., 1994, MNRAS, 267, 1020

Peebles P. J. E., 1993, Principles of Physical Cosmology. Princeton Univ. Press, Princeton, ISBN 0-691-07428-3

Pei Y. C., 1993, ApJ, 403, 7

Perlmutter S. et al., 1999, ApJ, 517, 565

Premadi P., Martel H., Matzner R., 1998a, ApJ, 493, 10

Premadi P., Martel H., Matzner R., 1998b, Abstracts of the 19th Texas Symposium on Relativistic Astrophysics and Cosmology, Paris, p. 536

Premadi P., Martel H., Matzner R., 1999, Proceedings of the 1998 International Conference on Numerical Astrophysics, Tokyo, p. 39

Rauch K. P., 1991, ApJ, 374, 83

Refsdal S., 1970, ApJ, 159, 357

Richstone D. O., Loeb A., Turner E. L., 1992, ApJ, 393, 477

Riess A. G. et al., 1998, AJ, 116, 1009

Schneider P., Ehlers J., Falco E. E., 1992, Gravitational Lenses. Springer-Verlag, ISBN 0-387-97070-3

Subramanian K., Cen R., Ostriker J. P., 2000, ApJ, 538, 528

Tomita K., 1998a, Prog. Theor. Phys., 99, 97

Tomita K., 1998b, astro-ph 9806003, preprint

Tomita K., 1998c, Prog. Theor. Phys., 100, 79

Viana P. T. P., Liddle A. R., 1996, MNRAS, 281, 323

Wambsganss J., Cen R., Xu G., Ostriker J. P., 1997, ApJ, 475, L81

Wambsganss J., Cen R., Ostriker J. P., 1998, ApJ, 494, 29

White M., Hu W., 2000, ApJ, 537, 1

APPENDIX A: GENERALIZATION OF THE DYER–ROEDER EQUATION

In Section 4 we presented the most simple form for the Dyer–Roeder equation (equation 34), which can be solved analytically for $\Omega_0 = 1$, $\lambda_0 = 0$, and arbitrary $\bar{\alpha}$. The general solution for the angular diameter distance between redshifts of z_1 and z_2, in such a cosmology, is well documented (see, e.g., Schneider et al. 1992) and from this solution the multiplying factors $D_d D_{ds}/D_s$ are easily obtained. However, this solution applies only to cosmologies with zero cosmological constant. We therefore generalized the form of the Dyer–Roeder equation to apply to the cosmologies being studied in this work. The following summary of this work is likely to be helpful to others working in this field.

We started from the generalized beam equation, quoted by Linder (1998a,b):

$$\frac{\mathrm{d}^2 D}{\mathrm{d}z^2} + [3 + q(z)](1+z)^{-1}\frac{\mathrm{d}D}{\mathrm{d}z}$$
$$+ \frac{3}{2}(1+z)^{-2}D\sum_s (1+s)\bar{\alpha}_s(z)\Omega_s(z) = 0. \qquad (A1)$$

In this equation,

$$q(z) = \frac{\frac{1}{2}\sum_s \Omega_s(0)(1+3s)(1+z)^{1+3s}}{\sum_s \Omega_s(0)(1+z)^{1+3s} - \left[\sum_s \Omega_s(0) - 1\right]} \qquad (A2)$$

is the deceleration parameter at redshift z, each value of s denotes a content component of the universe (for example, non-relativistic matter, radiation, vacuum energy, etc.), and $\bar{\alpha}_s$ and $\Omega_s(z)$ represent the smoothness parameter and the density parameter respectively, applicable to the component s, and redshift z. For two-component cosmologies, to which we have restricted our work, $s = 0$ for dust and $s = -1$ for the vacuum energy. When $s = 0$ only, equation (A1) reduces to the Dyer–Roeder equation immediately. Also, with two components only, the equation for the deceleration parameter at the present day, reduces from equation (A2) to the familiar form, $q_0 = \frac{1}{2}\Omega(0) - \lambda(0)$, where now we have used Ω and λ to represent the matter and vacuum energy density parameters respectively. Also, the Hubble parameter is, in general,

$$H(z) = H_0\left\{\sum_s \Omega_s(0)(1+z)^{3(1+s)} - \left[\sum_s \Omega_s(0) - 1\right](1+z)^2\right\}^{1/2}. \qquad (A3)$$

For a two-component universe this becomes

$$H(z) = H_0\{\Omega(0)(1+z)^3 + \lambda(0) - [\Omega(0) + \lambda(0) - 1](1+z)^2\}^{1/2}. \qquad (A4)$$

For two components only, the generalized beam equation (equation A1) is

$$\frac{\mathrm{d}^2 D}{\mathrm{d}z^2} + [3 + q(z)](1+z)^{-1}\frac{\mathrm{d}D}{\mathrm{d}z} + \frac{3}{2}(1+z)^{-2}D\bar{\alpha}(z)\Omega(z) = 0, \qquad (A5)$$

in which

$$q(z) = \frac{\frac{1}{2}[\Omega(0)(1+z) - 2\lambda(0)(1+z)^{-2}]}{\Omega(0)z + \lambda(0)(1+z)^{-2} - \lambda(0) + 1}, \qquad (A6)$$

$$\Omega(z) = \Omega(0)(1+z)^3[H(z)/H_0]^{-2}, \qquad (A7)$$

$$\frac{H(z)}{H_0} = \{\Omega(0)(1+z)^3 + \lambda(0) - [\Omega(0) + \lambda(0) - 1](1+z)^2\}^{1/2}, \qquad (A8)$$

and so

$$\Omega(z) = \Omega(0)(1+z)^3\{\Omega(0)(1+z)^3 + \lambda(0)$$
$$- [\Omega(0) + \lambda(0) - 1](1+z)^2\}^{-1}. \qquad (A9)$$

To solve equation (A5), boundary conditions

$$D(z_1, z_1) = 0, \qquad (A10)$$

and

$$\left.\frac{\mathrm{d}D(z_1, z)}{\mathrm{d}z}\right|_{z=z_1} = (1+z_1)\left[\frac{H(z_1)}{H_0}\right]^{-1} \qquad (A11)$$

are set, where the second condition is made by considering the form of the Hubble law for a fictitious observer at the redshift z_1.

However, we need values for the angular diameter distances between any arbitrary redshift values (not always based on $z = 0$)

in order to construct values for $D_\mathrm{d}D_\mathrm{ds}/D_\mathrm{s}$ at all the required evaluation positions. To do this, equation (A5) has to be generalized further to apply to any arbitrary redshift, and we can do this by changing the variable to

$$w \equiv \frac{1+z}{1+z_1} - 1. \tag{A12}$$

w then corresponds to the redshift of an object as if viewed by an observer at the arbitrary redshift z_1. Then, substituting the expression for $q(z)$ (equation A6), equation (A5) becomes, after some manipulation,

$$\frac{\mathrm{d}^2 D}{\mathrm{d}w^2}(1+z_1)^2 + \left\{ 3 + \frac{\frac{1}{2}[\Omega(0)x - 2\lambda(0)x^{-2}]}{\Omega(0)(x-1) + \lambda(0)x^{-2} - \lambda(0) + 1} \right\}$$

$$\times \frac{1}{x}\frac{\mathrm{d}D}{\mathrm{d}w}(1+z_1) + \frac{3}{2}D\bar{\alpha}$$

$$\times \left\{ \frac{\Omega(0)x}{\Omega(0)x^3 + \lambda(0) - [\Omega(0) + \lambda(0) - 1]x^2} \right\} = 0, \tag{A13}$$

with boundary conditions,

$$D(z_1, z_1) = 0, \tag{A14}$$

and

$$\left. \frac{\mathrm{d}D(z_1, w)}{\mathrm{d}w} \right|_{w=z_1} = (1+z_1)^{-1}\{\Omega(0)(1+z_1)^3 + \lambda(0)$$

$$- [\Omega(0) + \lambda(0) - 1](1+z_1)^2\}^{-1/2}. \tag{A15}$$

[In equation A13 we have written $x \equiv (1+w)/(1+z_1)$ for clarity.]

We have solved this equation numerically for all the cosmologies, checking carefully that the results are the same as the analytical values for the Einstien-de Sitter model. To solve it, we made further definitions to simplify the form of the equation. First, for clarity, we directly interchanged w and z, and made the following definitions.

$$a \equiv (1+z_1)^2, \tag{A16}$$

$$b \equiv \Omega(0)/(1+z_1), \tag{A17}$$

$$c \equiv 2\lambda(0)(1+z_1)^2, \tag{A18}$$

$$d \equiv 2\Omega(0)/(1+z_1), \tag{A19}$$

$$e \equiv 2 - 2\Omega(0) - 2\lambda(0), \tag{A20}$$

$$f \equiv \tfrac{3}{2}\bar{\alpha}\Omega(0)/(1+z_1), \tag{A21}$$

$$g \equiv \Omega(0)/(1+z_1)^3, \tag{A22}$$

$$h \equiv \lambda(0), \tag{A23}$$

$$i \equiv [\Omega(0) + \lambda(0) - 1]/(1+z_1)^2, \tag{A24}$$

and

$$j \equiv (1+z_1)^{-1}\{\Omega(0)(1+z_1)^3 + \lambda(0)$$

$$- [\Omega(0) + \lambda(0) - 1](1+z_1)^2\}^{-1/2}. \tag{A25}$$

Then the general two-component equation to solve is

$$\frac{\mathrm{d}^2 D}{\mathrm{d}z^2}a + \left[3 + \frac{b(1+z) - c(1+z)^{-2}}{d(1+z) + e + c(1+z)^{-2}} \right]a(1+z)^{-1}\frac{\mathrm{d}D}{\mathrm{d}z}$$

$$+ \frac{f(1+z)}{g(1+z)^3 + h - i(1+z)^2}D = 0, \tag{A26}$$

with boundary conditions

$$D(z_1, z_1) = 0, \tag{A27}$$

and

$$\left. \frac{\mathrm{d}D(z_1, z)}{\mathrm{d}z} \right|_{z=z_1} = j. \tag{A28}$$

Fig. 1 shows the result of solving equation (A26), with $\bar{\alpha} = 1$, in the different cosmologies, for a source redshift of $z_\mathrm{s} = 3.6$, and Fig. 2 shows the values of $r_\mathrm{d}r_\mathrm{ds}/r_\mathrm{s}$, also for $\bar{\alpha} = 1$. We have tabulated the ratios $R(\bar{\alpha} = 1)/R(\bar{\alpha} = 0)$ for the different cosmologies in Table 2.

This paper has been typeset from a TEX/LATEX file prepared by the author.